

# Development, Implementation, and Experimental Outdoor Evaluation of Quadcopter Controllers for Computationally Limited Embedded Systems

Juan Paredes<sup>a,1,\*</sup>, Prashin Sharma<sup>a,2</sup>, Brian Ha<sup>a,3</sup>, Manuel Lanchares<sup>a,4</sup>, Ella Atkins<sup>a,5</sup>, Peter Gaskell<sup>a,6</sup>, Ilya Kolmanovsky<sup>a,7</sup>

<sup>a</sup>University of Michigan, Ann Arbor, Michigan, 48109, USA

---

## Abstract

Quadcopters are increasingly used for applications ranging from hobby to industrial products and services. This paper serves as a tutorial on the design, simulation, implementation, and experimental outdoor testing of digital quadcopter flight controllers, including Explicit Model Predictive Control, Linear Quadratic Regulator, and Proportional Integral Derivative. A quadcopter was flown in an outdoor testing facility and made to track an inclined, circular path at different tangential velocities under ambient wind conditions. Controller performance was evaluated via multiple metrics, such as position tracking error, velocity tracking error, and onboard computation time. Challenges related to the use of computationally limited embedded hardware and flight in an outdoor environment are addressed with proposed solutions.

*Keywords:* unmanned aerial vehicles, quadcopters, digital controller implementation, outdoor flight, computationally limited, embedded systems

---

## 1. Introduction

As autonomous multicopters or drones become more prevalent, emphasis on their performance and safety grows. Small quadcopters are now consid-

ered frequently for commercial use. Their performance depends not only on their design but also on their flight control system. Numerous approaches to quadcopter control have been reported in the literature. Practical implementation topics such as in situ sensor calibration, vehicle parameter modeling, controller software, and real-time execution on computationally limited platforms are of interest.

This paper investigates classical and modern techniques for quadrotor flight control. The following control algorithms are implemented and evaluated: Proportional-Derivative (PD), Proportional-Integral-Derivative (PID), Linear-Quadratic Regulator (LQR), LQR with Integrators (LQR-I), and Explicit Model Predictive Control (E-MPC). A thorough tutorial of quadrotor flight controller design, simulation, implementation, and evaluation is presented with the following contributions:

- Details of the design, software implementation, and tuning of the quadcopter controllers with emphasis on implementation in a computationally limited embedded platform.
- Experimental results from outdoor flight tests including a performance comparison of each

---

\*Corresponding author

*Email addresses:* [jparedes@umich.edu](mailto:jparedes@umich.edu) (Juan Paredes), [prashinr@umich.edu](mailto:prashinr@umich.edu) (Prashin Sharma), [brian.stephen.ha@gmail.com](mailto:brian.stephen.ha@gmail.com) (Brian Ha), [lanchares@gatech.edu](mailto:lanchares@gatech.edu) (Manuel Lanchares), [ematkins@umich.edu](mailto:ematkins@umich.edu) (Ella Atkins), [pgaskell@umich.edu](mailto:pgaskell@umich.edu) (Peter Gaskell), [ilya@umich.edu](mailto:ilya@umich.edu) (Ilya Kolmanovsky)

<sup>1</sup>PhD Candidate, Aerospace Engineering, 1320 Beal Ave, Ann Arbor, MI 48109

<sup>2</sup>PhD Candidate, Robotics Institute, 1320 Beal Ave, Ann Arbor, MI 48109, AIAA Student Member

<sup>3</sup>MS Graduate, Aerospace Engineering, 1320 Beal Ave, Ann Arbor, MI 48109

<sup>4</sup>PhD Candidate, Aerospace Engineering, Georgia Institute of Technology, North Ave NW, Atlanta, GA 30332. This work was done during his two-year affiliation as an MS Student with the Department of Aerospace Engineering, University of Michigan, 1320 Beal Ave, Ann Arbor, MI 48109

<sup>5</sup>Professor, Aerospace Engineering, 1320 Beal Ave, Ann Arbor, MI 48109, AIAA Fellow

<sup>6</sup>Adjunct Research Investigator, Robotics Institute, 2455 Hayward St, Ann Arbor, MI 48109

<sup>7</sup>Professor, Aerospace Engineering, 1320 Beal Ave, Ann Arbor, MI 48109, AIAA Associate Fellow

Table 1: Nomenclature

$\hat{i}^i, \hat{j}^i, \hat{k}^i$	Orthogonal unit vectors aligned with the inertial coordinate frame
$\hat{i}^b, \hat{j}^b, \hat{k}^b$	Orthogonal unit vectors aligned with the body (quadcopter) coordinate frame
$x^i, y^i, z^i$	Position of the quadcopter geometric center along the $\hat{i}^i, \hat{j}^i, \hat{k}^i$ axes respectively [m]
$\dot{x}^i, \dot{y}^i, \dot{z}^i$	Velocity of the quadcopter geometric center along the $\hat{i}^i, \hat{j}^i, \hat{k}^i$ axes respectively [m/s]
$\phi, \theta, \psi$	Euler angles, quadcopter rotations around the $\hat{i}^i, \hat{j}^i$ and $\hat{k}^i$ axes respectively [rad]
$\omega_x^b, \omega_y^b, \omega_z^b$	Quadcopter rotation rates about the $\hat{i}^b, \hat{j}^b$ and $\hat{k}^b$ axes respectively [rad/s]
$r_x^i, r_y^i, r_z^i$	Reference signals for position of the quadcopter geometric center along the $\hat{i}^i, \hat{j}^i, \hat{k}^i$ axes respectively [m]
$r_{\dot{x}}^i, r_{\dot{y}}^i, r_{\dot{z}}^i$	Reference signals for velocity of the quadcopter geometric center along the $\hat{i}^i, \hat{j}^i, \hat{k}^i$ axes respectively [m/s]
$r_{\psi}^i, r_{\dot{\psi}}^i$	Reference signals for yaw and yaw rate respectively [rad, rad/s]
$T$	Total vertical thrust of quadcopter rotors in body frame [N]
$T_{\text{hov}}$	Total vertical thrust required by quadcopter to remain in hover condition for $\phi = \theta = 0$ rad [N]
$\tau_x, \tau_y, \tau_z$	Torque of quadcopter rotors around the $\hat{i}^b, \hat{j}^b, \hat{k}^b$ axes respectively [N·m]
$d$	Distance of each rotor to the geometric center of the quadcopter [m]
$\omega_{\text{ss}, i}$	Steady state propulsor angular velocity $i \in \{1, 2, 3, 4\}$ [RPM]
$\sigma_i$	Normalized throttle signal in $[0, 1]$ for motor $i \in \{1, 2, 3, 4\}$
$\omega_b$	Steady state propeller angular velocity bias [RPM]
$C_R$	Steady state propeller angular velocity parameter [RPM]
$T_m$	Time constant of propulsor first-order dynamics
$\omega_i$	Propulsor angular velocity $i \in \{1, 2, 3, 4\}$ . [RPM]
$C_T$	Rotor thrust coefficient [kg·m]
$C_M$	Rotor moment coefficient [kg·m <sup>2</sup> ]
$T_i$	Thrust generated by propulsor $i \in \{1, 2, 3, 4\}$ [N]
$M_i$	Moment magnitude generated by propulsor $i \in \{1, 2, 3, 4\}$ [N·m]
$m$	Quadcopter mass [kg]
$J_{xx}, J_{yy}, J_{zz}$	Quadcopter moment of inertia around the $\hat{i}^b, \hat{j}^b, \hat{k}^b$ axes, respectively [kg·m <sup>2</sup> ]
$T_s$	Sampling time [s]
$s\phi, c\phi, t\phi,$	Sine, cosine, and tangent of angle $\phi$ , respectively.

controller's ability to follow an inclined, circular path under varying ambient conditions.

- Design and implementation of ancillary autopilot components such as state estimators to support full state feedback and actuator mapping.

Quadrotor or quadcopter modelling and control

has been frequently studied in the literature. In Bouabdallah and Siegwart (2007), quadcopter aerodynamics were modelled using blade element and momentum theory; a back-stepping, integral controller was used for attitude and position control. Maximum reference deviations of 3 cm and 20 cm were observed for attitude and position, respectively. Similarly, in Hoffmann et al. (2007), various aerodynamic effects experienced by quadcopters at high speeds with wind disturbances were presented and validated through thrust test stand experiments and flight tests. In contrast to Bouabdallah and Siegwart (2007), a simple PID controller was used for position and attitude control. Powers et al. (2015) showed a simplified lumped parameter model for quadcopter motor dynamics and described the design and implementation of continuous-time LQR and nonlinear controllers. A nano quadcopter with a linear controller was commanded in tests to fly in a circular trajectory of radius 0.5 m with a maximum acceleration of 0.008 m/s<sup>2</sup>. Errors of 10 cm and 1 cm were observed along the horizontal and vertical planes, respectively.

Quadcopter PID control is studied in Dong et al. (2013) and Bolandi et al. (2013). In both references, quadcopter dynamics were linearized and treated as decoupled around each axis to facilitate the implementation of single input single output (SISO) control techniques. In Dong et al. (2013), the PID controller was designed using root locus analysis and Ziegler-Nichols tuning, while Bolandi et al. (2013) used the Direct Synthesis method. Outdoor trajectory tracking flight tests were conducted in Dong et al. (2013) with a maximum position error of 50 cm, but no discussion of velocity tracking error was presented.

To achieve improved performance, multivariable control techniques such as LQR have also been considered. Reyes-Valeria et al. (2013) designed a gain scheduled LQR controller with gains calculated for two different situations: (1) Quadcopter far from the reference, and (2) Quadcopter was already closely tracking the reference state. Another implementation of LQR can be found in Heng et al. (2015) which addressed actuator saturation.

Due to its ability to handle constraints, Model Predictive Control (MPC) has been pursued for multicopters, especially in cases when substantial computational power is available. Kamel et al. (2017) implemented linear, nonlinear, and robust MPC schemes for a hexacopter with a NUCi7 computer onboard. Liu et al. (2015) developed an ex-

PLICIT MPC scheme for trajectory tracking and verified it in simulation. Their approach exploited differential flatness and Bezier curves and was solved offline using a quadratic programming technique. An efficient MPC scheme with a reduced computational footprint was proposed in Abdolhosseini et al. (2013) for controlling quadcopters. An unconstrained MPC law was implemented on a computer embedded on a quadcopter in Bangura and Mahony (2014).

MPC was applied to a simplified, linear dynamics model derived via feedback linearization. This yielded desired thrust, rotation rates, and angular accelerations, which were subsequently regulated by a high-gain attitude controller obtained by exploiting quadcopter attitude dynamics.

The robustness of quadcopter controllers to disturbances such as wind gusts has also been studied. In Waslander and Wang (2009), a wind compensator was added to the outer PID loop to reject wind effects. This decreased position error from 40 cm to 10 cm. A constrained, finite-time optimal control scheme was developed and experimentally validated in Alexis et al. (2010). The quadcopter was able to effectively achieve the desired set point in the presence of wind gusts.

This paper synthesizes multiple quadcopter control laws and evaluates them in simulation and in flight testing. Though organized as a tutorial, this paper also offers novelty in its careful experimental evaluation and comparison of a diverse control law suite. The organization of this paper is as follows. Quadcopter design and system modelling are presented in Section 2 followed by guidance, navigation, and control strategies in Section 3. The state estimation algorithm is presented in Section 3.2. Formulations for all tested controllers are provided in Section 4 with simulation results of each controller presented in Section 5. The experimental setup and results from outdoor flight tests are provided in Sections 6 and 7, respectively. Results are discussed in Section 8 with a brief conclusion provided in Section 9. Nomenclature used in this paper is summarized in Table 1.

## 2. System Description

### 2.1. Hardware

This section describes the tested hardware platform. The assembled quadcopter is shown in Fig. 1. The onboard Beaglebone Blue Linux computer

features a 1GHz ARM <sup>®</sup> Cortex-A8 processor with eight servomotor outputs, an MPU9250 Inertial Measurement Unit (IMU) with three-axis angular rate gyro, accelerometer, and magnetic field sensors, a WiFi 2.4 GHz transceiver module, and UART interfaces for serial communications. The pre-installed Robot Control Library was used to facilitate controller C code implementation. The controller code was required to complete all calculations within a 0.005 second time interval between system interrupts ( $T_s = 0.005$  s). The Beaglebone Blue interfaced with all peripherals including sensors, Pulse Width Modulation (PWM) signals to control motor speeds, and communication links. An IMU measured angular rates and orientation of the body frame with respect to a flat-Earth inertial frame gravity vector. The Wi-Fi transceiver module allowed two-way communication between the embedded board and a ground station computer. An xBee modem connected to a UART interface to reliably update position and heading measurements from a Qualisys Motion Capture (MOCAP) camera system. Finally, a Radio Control (RC) receiver obtained commands from a RC Controller to initiate/terminate tests and for manual backup control as described further in Section 6.

A DJI Flamewheel F450 ARF kit was used for the quadcopter frame, with AIR 2213/920KV brushless DC motors and APC (8 x 4.5) propellers for the propulsion units. The system was powered by a 3S 3000 mAh 35C LiPo battery. A Power Distribution Board (PDB) distributed 5V and 12V to the embedded board and the motors, respectively. Each motor was connected to an AIR 20A Electronic Speed Controller (ESC) controlled by Beaglebone PWM signals. 3D printed propeller guards, originally designed in Romano et al. (2019), were attached at the base of each motor and connected

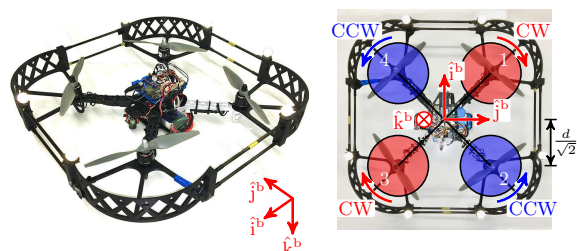


Figure 1: Experimental quadcopter based on a DJI Flamewheel F450 frame with custom propeller guards and avionics mounts. Motion capture markers are placed on propeller guards for increased camera visibility.

by carbon fiber tubes to provide protection for propellers and users. MOCAP was used to determine the 3D location and heading of the quadcopter with targets placed on top of the propeller guards. The quadcopter and body-fixed coordinate frame are shown in Fig. 1.

## 2.2. Quadcopter Dynamics and System Modelling

This section describes the quadcopter model and is based on content from Chapters 5 and 6 of Quan (2017).

### 2.2.1. Quadcopter Configuration

The body-fixed frame (Fig. 1) is composed of orthogonal unit vectors  $\hat{i}^b, \hat{j}^b, \hat{k}^b$ . The  $\hat{i}^b$  axis points forward on the quadcopter, the  $\hat{k}^b$  axis points down, and the  $\hat{j}^b$  axis points right to satisfy a right-hand convention. Let  $\hat{i}^i, \hat{j}^i, \hat{k}^i$  denote orthogonal unit vectors defining an inertial coordinate frame, such that  $\hat{k}^i$  points toward the ground. Let  $\psi, \theta, \phi$  denote yaw, pitch, and roll Euler angles, respectively. Following a  $\psi \rightarrow \theta \rightarrow \phi$  rotation ordering convention, the relation between inertial axes  $\hat{i}^i, \hat{j}^i, \hat{k}^i$  and the body-fixed axes  $\hat{i}^b, \hat{j}^b, \hat{k}^b$  is given by

$$\begin{bmatrix} \hat{i}^i \\ \hat{j}^i \\ \hat{k}^i \end{bmatrix} = \mathbf{R}_{b/i} \begin{bmatrix} \hat{i}^b \\ \hat{j}^b \\ \hat{k}^b \end{bmatrix}. \quad (1)$$

where  $\mathbf{R}_{b/i}$  is the rotation matrix from body-fixed frame to inertial frame, such that

$$\mathbf{R}_{b/i} \triangleq \begin{bmatrix} c\psi & c\psi & c\psi & s\theta & s\phi - s\psi & c\phi & c\psi & s\theta & c\phi + s\psi & s\phi \\ c\theta & s\psi & s\psi & s\theta & s\phi + c\psi & c\phi & s\psi & s\theta & c\phi - c\psi & s\phi \\ -s\theta & & & s\phi & c\theta & & c\phi & c\theta & & \end{bmatrix}. \quad (2)$$

Fig. 1 displays the X-configuration chosen for the quadcopter and the direction of rotation of each propeller. Propellers 2 and 4 (in blue) rotate counterclockwise (CCW) and propellers 1 and 3 (in red) rotate clockwise (CW).

### 2.2.2. Propulsor Dynamics

The dynamics model for each propulsion unit (motor with propeller) is depicted by the block diagram in Fig. 2. Let indices  $i \in \{1, 2, 3, 4\}$  denote each propulsor as shown in Fig. 1. Each motor was driven by a normalized throttle signal  $\sigma_i \in [0, 1]$ , such that  $\sigma_i = 0$  gives no rotation and  $\sigma_i = 1$  yielded the maximum rotation speed for propulsor  $i$ .  $\sigma_i$  represents the duty cycle of the PWM signal sent by the controller to propulsor  $i$ . The steady

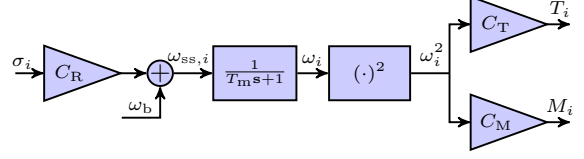


Figure 2: Propulsor dynamics block diagram. The normalized control signal  $\sigma_i$  (PWM duty cycle) is used to determine output thrust magnitude  $T_i$  and torque magnitude  $\tau_i$ .

state angular velocity of propulsor  $i$  in RPM,  $\omega_{ss,i}$ , is given by

$$\omega_{ss,i} = C_R \sigma_i + \omega_b, \quad (3)$$

where  $C_R$  and  $\omega_b$  define the steady state characteristics of each propulsor. The transient response of propulsor angular velocity  $\omega_i$  is modeled by a first-order, low pass filter with time constant  $T_m$ , such that the transfer function of a model with input  $\omega_{ss,i}$  and output  $\omega_i$  is given by

$$\omega_i = \frac{1}{T_m s + 1} \omega_{ss,i}, \quad (4)$$

where  $s$  is the Laplace transform complex variable. Finally, the thrust and torque magnitudes generated by the  $i^{th}$  propulsor,  $T_i$  and  $M_i$  respectively, are given by

$$T_i = C_T \omega_i^2, \quad (5)$$

$$M_i = C_M \omega_i^2, \quad (6)$$

where  $C_T$  and  $C_M$  are parameters that characterize each propeller's aerodynamic properties.

### 2.2.3. Quadcopter Inputs and Mixing Matrix

Assuming the quadcopter body is rigid, the propulsors generate a total thrust  $T$  in direction of  $-\hat{k}^b$  with three torque components  $\tau_x$ ,  $\tau_y$  and  $\tau_z$  about  $\hat{i}^b$ ,  $\hat{j}^b$ , and  $\hat{k}^b$  axes, respectively. Each propulsor generates a thrust in the direction of  $-\hat{k}^b$  and a torque aligned with  $\hat{k}^b$ , in the direction opposite to its rotation. Hence, it follows from (5) and (6) that

$$\begin{bmatrix} T \\ \tau_x \\ \tau_y \\ \tau_z \end{bmatrix} = \begin{bmatrix} T_1 + T_2 + T_3 + T_4 \\ \frac{\sqrt{2}}{2} d (-T_1 - T_2 + T_3 + T_4) \\ \frac{\sqrt{2}}{2} d (T_1 - T_2 - T_3 + T_4) \\ -M_1 + M_2 - M_3 + M_4 \end{bmatrix} = \begin{bmatrix} C_T & C_T & C_T & C_T \\ -C_T & -C_T & C_T & C_T \\ C_T & -C_T & -C_T & C_T \\ -C_M & C_M & -C_M & C_M \end{bmatrix} \begin{bmatrix} \omega_1^2 \\ \omega_2^2 \\ \omega_3^2 \\ \omega_4^2 \end{bmatrix}, \quad (7)$$

where  $d = 0.17$  m is the distance from each rotor to the geometric center and  $C_T \triangleq \frac{\sqrt{2}}{2} d C_{T_i}$ . The

rightmost matrix of (7) is denoted the mixing matrix and describes the linear transformation from squared motor angular velocities to quadcopter system input.

#### 2.2.4. Quadcopter System Dynamics

The quadcopter dynamics model is derived under the assumptions that the quadcopter body is rigid, its mass properties remain constant during operation, and the geometric center and the center of gravity are located in the same position. It is assumed that no aerodynamic forces or moments act upon the quadcopter apart from the thrust and torque generated by each propulsor. In practice, the quadcopter body drag and blade flapping have a significant impact on the dynamics of the quadcopter at high flight velocities and in outdoor environments, as is stated in Huang et al. (2009). Nonetheless, these assumptions allow the resulting model to achieve a balance between simplicity and accuracy for the purpose of designing a control strategy. Let  $m$  be the mass the quadcopter in kg,  $J \triangleq \text{diag}([J_{xx} J_{yy} J_{zz}]^T)$  be the inertia tensor with respect to the body fixed frame in  $\text{kg} \cdot \text{m}^2$ . Let  $X \in \mathbb{R}^{12}$  be the system state vector and  $U \in \mathbb{R}^4$  be the system input vector, such that

$$X \triangleq [x^i \ y^i \ z^i \ \dot{x}^i \ \dot{y}^i \ \dot{z}^i \ \phi \ \theta \ \psi \ \omega_x^b \ \omega_y^b \ \omega_z^b]^T, \\ U \triangleq [T \ \tau_x \ \tau_y \ \tau_z]^T,$$

where  $x^i, y^i, z^i$  represent quadcopter position in the inertial frame,  $\dot{x}^i, \dot{y}^i, \dot{z}^i$  represent its velocity vector in the same frame,  $\phi, \theta, \psi$  are the Euler angles representing the orientation of body-fixed frame with respect to inertial frame axes, and  $\omega_x^b, \omega_y^b, \omega_z^b$  are the components of quadcopter angular velocity expressed in the body-fixed frame. The nonlinear model for the quadcopter dynamics is

$$\frac{d}{dt}X = f_{\text{quad}}(X, U). \quad (8)$$

Assuming the only forces acting on the quadcopter center of gravity are its weight  $mg$  and total thrust  $T$ , Newton's Second Law yields:

$$\frac{d}{dt} \begin{bmatrix} \dot{x}^i \\ \dot{y}^i \\ \dot{z}^i \end{bmatrix} = \begin{bmatrix} 0 \\ 0 \\ g \end{bmatrix} - \text{R}_{b/i} \begin{bmatrix} 0 \\ 0 \\ \frac{T}{m} \end{bmatrix} = \begin{bmatrix} 0 \\ 0 \\ g \end{bmatrix} - \begin{bmatrix} c\psi \ s\theta c\phi + s\psi s\phi \\ s\psi s\theta c\phi - c\psi s\phi \\ c\theta c\phi \end{bmatrix} \frac{T}{m}. \quad (9)$$

Furthermore, considering the torques  $\tau_x, \tau_y, \tau_z$  generated by the propulsors, it follows from the classi-

cal Euler equations of rotational dynamics that

$$\frac{d}{dt} \begin{bmatrix} \omega_x^b \\ \omega_y^b \\ \omega_z^b \end{bmatrix} = \begin{bmatrix} \frac{\tau_x}{J_{xx}} \\ \frac{\tau_y}{J_{yy}} \\ \frac{\tau_z}{J_{zz}} \end{bmatrix} + \begin{bmatrix} \frac{J_{yy} - J_{zz}}{J_{xx}} \omega_y^b \omega_z^b \\ \frac{J_{zz} - J_{xx}}{J_{yy}} \omega_x^b \omega_z^b \\ \frac{J_{xx} - J_{yy}}{J_{zz}} \omega_x^b \omega_y^b \end{bmatrix}. \quad (10)$$

Finally, the relation between angular velocity vector components and time rate of changes of 3-2-1 Euler angles is given by

$$\begin{bmatrix} \dot{\phi} \\ \dot{\theta} \\ \dot{\psi} \end{bmatrix} = \begin{bmatrix} 1 & t\theta s\phi & t\theta c\phi \\ 0 & c\phi & -s\phi \\ 0 & s\phi/c\theta & c\phi/c\theta \end{bmatrix} \begin{bmatrix} \omega_x^b \\ \omega_y^b \\ \omega_z^b \end{bmatrix}. \quad (11)$$

Equation (9) describes the effects of gravity, attitude, and total thrust  $T$  on three-dimensional quadcopter motion. Note that total thrust vector  $T$  is along the  $\hat{k}^b$  vector so its projection onto inertial frame axes requires multiplication by a rotation matrix per Eq. (9). Equation (10) describes the effect of torques  $\tau_x, \tau_y$  and  $\tau_z$  on the angular velocity. Gyroscopic torques caused by motor rotations are considered negligible and are thus not included in the present model. Eq. (11) relates Euler angle rates and angular velocity components as a function of quadcopter attitude. These nonlinear equations are used for simulations and to derive linearized equations for controller design.

#### 2.2.5. Linearized System Dynamics

To design LQR, LQR-I, and MPC controllers, the nonlinear model presented above is linearized around an equilibrium point corresponding to hover. As will be shown in test results, a linearized model is sufficient as a basis for controller design even when tracking a trajectory which deviates substantially from hover conditions.

Let  $X_{\text{hov}} \in \mathbb{R}^{12}$  be the system state vector in hover conditions and  $U_{\text{hov}} \in \mathbb{R}^4$  be the system input vector in hover conditions, such that

$$X_{\text{hov}} \triangleq [x_{\text{hov}}^i \ y_{\text{hov}}^i \ z_{\text{hov}}^i \ \dot{x}_{\text{hov}}^i \ \dot{y}_{\text{hov}}^i \ \dot{z}_{\text{hov}}^i \\ \phi_{\text{hov}} \ \theta_{\text{hov}} \ \psi_{\text{hov}} \ \omega_{x,\text{hov}}^b \ \omega_{y,\text{hov}}^b \ \omega_{z,\text{hov}}^b]^T \\ = [x_{\text{hov}}^i \ y_{\text{hov}}^i \ z_{\text{hov}}^i \ 0 \ 0 \ 0 \ 0 \ 0 \ 0 \ 0 \ 0 \ 0]^T, \\ U_{\text{hov}} \triangleq [T_{\text{hov}} \ \tau_{x,\text{hov}} \ \tau_{y,\text{hov}} \ \tau_{z,\text{hov}}]^T = [mg \ 0 \ 0 \ 0]^T.$$

Let  $\delta X \in \mathbb{R}^{12}$  and  $\delta U \in \mathbb{R}^4$  be the state and input deviations from hover, respectively, such that  $\delta X = X - X_{\text{hov}}$  and  $\delta U = U - U_{\text{hov}}$ . Since  $\phi_{\text{hov}} = \theta_{\text{hov}} = \psi_{\text{hov}} = 0$ , the linearization is performed assuming that the body-fixed and the inertial frames are aligned. Furthermore, it follows

from Eq. (11) that, under hover conditions, the Euler angle rates and the body angular velocities are the same. Hence, it follows that

$$\begin{aligned} \delta X &\triangleq [\delta x^b \ \delta y^b \ \delta z^b \ \delta \dot{x}^b \ \delta \dot{y}^b \ \delta \dot{z}^b \\ &\quad \delta \phi \ \delta \theta \ \delta \psi \ \delta \dot{\phi} \ \delta \dot{\theta} \ \delta \dot{\psi}]^T \\ \delta U &\triangleq [\delta T \ \delta \tau_x \ \delta \tau_y \ \delta \tau_z]^T = [\delta T \ \tau_x \ \tau_y \ \tau_z]^T. \end{aligned}$$

Given the nonlinear representation of the dynamics in (8), the linearized quadcopter dynamics model takes the form

$$\begin{aligned} \frac{d}{dt} \delta X &= \left. \frac{\partial f_{\text{quad}}(X, U)}{\partial X} \right|_{X=X_{\text{hov}}, U=U_{\text{hov}}} \delta X \\ &+ \left. \frac{\partial f_{\text{quad}}(X, U)}{\partial U} \right|_{X=X_{\text{hov}}, U=U_{\text{hov}}} \delta U. \end{aligned} \quad (12)$$

Note that linearization decomposes the dynamics of the nonlinear model into six sub-models. Each sub-model is defined by its generalized state  $\delta \mathbb{X}$ , its time derivative  $\delta \dot{\mathbb{X}}$ , a parameter  $K_\delta$ , a generalized input  $\delta \mathbb{U}$ , and dynamic equations of the form

$$\frac{d}{dt} \begin{bmatrix} \delta \mathbb{X} \\ \delta \dot{\mathbb{X}} \end{bmatrix} = \begin{bmatrix} 0 & 1 \\ 0 & 0 \end{bmatrix} \begin{bmatrix} \delta \mathbb{X} \\ \delta \dot{\mathbb{X}} \end{bmatrix} + \begin{bmatrix} 0 \\ K_\delta \end{bmatrix} \delta \mathbb{U}. \quad (13)$$

For  $\delta \mathbb{X} = \delta x^b, \delta \mathbb{U} = \delta \theta$  and  $K_\delta = -g$ . For  $\delta \mathbb{X} = \delta y^b, \delta \mathbb{U} = \delta \phi$  and  $K_\delta = g$ . For  $\delta \mathbb{X} = \delta z^b, \delta \mathbb{U} = \delta T$  and  $K_\delta = -\frac{1}{m}$ . For  $\delta \mathbb{X} = \delta \phi, \delta \mathbb{U} = \tau_y$  and  $K_\delta = \frac{1}{J_{yy}}$ . For  $\delta \mathbb{X} = \delta \theta, \delta \mathbb{U} = \tau_x$  and  $K_\delta = \frac{1}{J_{xx}}$ . For  $\delta \mathbb{X} = \delta \psi, \delta \mathbb{U} = \tau_z$  and  $K_\delta = \frac{1}{J_{zz}}$ .

### 2.2.6. Discretized Linearized System Dynamics

The linearized model in the previous section is discretized in order to design digital controllers. Let  $k$  be the sample index, and define discrete-time state vector  $X_k$  and input vector  $U_k$  such that

$$\begin{aligned} \delta X_k &\triangleq [\delta x_k^b \ \delta y_k^b \ \delta z_k^b \ \delta \dot{x}_k^b \ \delta \dot{y}_k^b \ \delta \dot{z}_k^b \\ &\quad \delta \phi_k \ \delta \theta_k \ \delta \psi_k \ \delta \dot{\phi}_k \ \delta \dot{\theta}_k \ \delta \dot{\psi}_k]^T, \\ \delta U_k &\triangleq [\delta T_k \ \tau_{x,k} \ \tau_{y,k} \ \tau_{z,k}]^T. \end{aligned}$$

Assuming a zero-order hold for the input and a sampling period of  $T_s$ , each of the six sub-models (13) is converted to discrete-time, with the discrete-time models given by

$$\begin{bmatrix} \delta \mathbb{X}_{k+1} \\ \delta \dot{\mathbb{X}}_{k+1} \end{bmatrix} = \begin{bmatrix} 1 & T_s \\ 0 & 1 \end{bmatrix} \begin{bmatrix} \delta \mathbb{X}_k \\ \delta \dot{\mathbb{X}}_k \end{bmatrix} + B_{T_s} \delta U_k, \quad (14)$$

where  $B_{T_s}$  is a 2-by-1 matrix. For  $\delta \mathbb{X}_k = \delta x_k^b, \delta \mathbb{U}_k = \delta \theta_k$  and  $B_{T_s} = -g \begin{bmatrix} \frac{T_s^2}{2} & T_s \end{bmatrix}^T$ . For

$$\begin{aligned} \delta \mathbb{X}_k &= \delta y_k^b, \delta \mathbb{U}_k = \delta \phi_k \text{ and } B_{T_s} = g \begin{bmatrix} \frac{T_s^2}{2} & T_s \end{bmatrix}^T. \text{ For} \\ \delta \mathbb{X}_k &= \delta z_k^b, \delta \mathbb{U}_k = \delta T_k \text{ and } B_{T_s} = -\begin{bmatrix} \frac{T_s^2}{2m} & \frac{T_s}{m} \end{bmatrix}^T. \text{ For} \\ \delta \mathbb{X}_k &= \delta \phi_k, \delta \mathbb{U}_k = \tau_{y,k} \text{ and } B_{T_s} = \begin{bmatrix} \frac{T_s^2}{2J_{yy}} & \frac{T_s}{J_{yy}} \end{bmatrix}^T. \text{ For} \\ \delta \mathbb{X}_k &= \delta \theta_k, \delta \mathbb{U}_k = \tau_{x,k} \text{ and } B_{T_s} = \begin{bmatrix} \frac{T_s^2}{2J_{xx}} & \frac{T_s}{J_{xx}} \end{bmatrix}^T. \text{ For} \\ \delta \mathbb{X}_k &= \delta \psi_k, \delta \mathbb{U}_k = \tau_{z,k} \text{ and } B_{T_s} = \begin{bmatrix} \frac{T_s^2}{2J_{zz}} & \frac{T_s}{J_{zz}} \end{bmatrix}^T. \end{aligned}$$

### 2.2.7. System Model Parameter Estimation

A summary of the estimated model parameters is displayed in Table 2. Parameters  $C_T, C_M, C_R, \omega_b$  and  $T_m$  were obtained via dynamometer tests performed on all propulsor systems, as described in Section 6.3.4 of Quan (2017). The value of  $d$  was determined by measuring the distance from the center of a propulsor to the geometric center of the quadcopter. The value of  $m$  was measured using a scale and  $J_{xx}, J_{yy}$  and  $J_{zz}$  were determined by performing a bifilar pendulum test, as described in Section 6.3.3 of Quan (2017). Finally, the value of the sampling period  $T_s$  was chosen as the fastest one available on the chosen embedded system. More details of parameter estimation techniques are given in Appendix A.

Table 2: System Model Parameters

Parameter	Value	Units
$C_T$	$5.724165 \cdot 10^{-8}$	kg.m
$C_M$	$8.881631 \cdot 10^{-10}$	kg.m <sup>2</sup>
$C_R$	$9.9573 \cdot 10^3$	1/s
$\omega_b$	12.3517	1/s
$T_m$	0.245217	N/A
$d$	0.17	m
$m$	1.062	kg
$J_{xx}$	$1.07 \cdot 10^{-2}$	kg.m <sup>2</sup>
$J_{yy}$	$1.11 \cdot 10^{-2}$	kg.m <sup>2</sup>
$J_{zz}$	$2.29 \cdot 10^{-2}$	kg.m <sup>2</sup>
$T_s$	0.05	s

## 3. Guidance, Navigation, and Control

The block diagram representing quadcopter guidance, navigation, and control is shown in Fig. 3. Let  $T_s$  be the sampling period,  $r \triangleq \begin{bmatrix} r_x^i & r_y^i & r_z^i & r_\psi^i & r_{\dot{x}}^i & r_{\dot{y}}^i & r_{\dot{z}}^i & r_{\dot{\psi}}^i \end{bmatrix}$  be the reference signal vector including setpoints for position  $(r_x^i, r_y^i, r_z^i)$ , velocity  $(r_{\dot{x}}^i, r_{\dot{y}}^i, r_{\dot{z}}^i)$ ,

yaw angle and yaw rate  $(r_\psi^i, \dot{r}_\psi^i)$ , and  $r_k \triangleq [r_{x,k}^i \ r_{y,k}^i \ r_{z,k}^i \ r_{\psi,k}^i \ r_{\dot{x},k}^i \ r_{\dot{y},k}^i \ r_{\dot{z},k}^i \ r_{\dot{\psi},k}^i]$  be the sampled reference signal vector, such that  $r_k = r(kT_s)$ . Let  $Y$  be the vector of quadcopter system output signals and  $Y_k$  be the vector of sampled sensor measurements such that  $Y_k = Y(kT_s)$ . At each iteration, the State Estimator provides a sampled estimate of state vector  $X_k$ , such that  $X_k = X(kT_s)$ . Due to the decomposition resulting from model linearization, the digital controller requires position and velocity states and references to be aligned with the axes of the frame obtained by rotating the  $\hat{i}^i$  and  $\hat{j}^i$  axes by  $\psi$  around the  $\hat{k}^i$  axis. Hence, a Yaw Alignment procedure must be performed to obtain aligned reference and state vectors  $r_k^\psi \triangleq [r_{x,k}^\psi \ r_{y,k}^\psi \ r_{z,k}^i \ r_{\psi,k}^\psi \ r_{\dot{x},k}^\psi \ r_{\dot{y},k}^\psi \ r_{\dot{z},k}^i \ r_{\dot{\psi},k}^i]$  and  $X_k^\psi \triangleq [x_k^\psi \ y_k^\psi \ z_k^i \ \dot{x}_k^\psi \ \dot{y}_k^\psi \ \dot{z}_k^i \ \phi_k \ \theta_k \ \psi_k \ \dot{\phi}_k \ \dot{\theta}_k \ \dot{\psi}_k]^\top$ , respectively. The following transforms  $[x_k^i \ y_k^i]^\top$  into  $[x_k^\psi \ y_k^\psi]^\top$ :

$$\begin{bmatrix} x_k^\psi \\ y_k^\psi \end{bmatrix} = \begin{bmatrix} c\psi & s\psi \\ -s\psi & c\psi \end{bmatrix} \begin{bmatrix} x_k^i \\ y_k^i \end{bmatrix}. \quad (15)$$

The same transformation is applied for transforming  $[\dot{x}_k^i \ \dot{y}_k^i]^\top$ ,  $[r_{x,k}^i \ r_{y,k}^i]^\top$ , and  $[r_{\dot{x},k} \ r_{\dot{y},k}]^\top$  into  $[x_k^\psi \ y_k^\psi]^\top$ ,  $[\dot{x}_k^\psi \ \dot{y}_k^\psi]^\top$ ,  $[r_{x,k}^\psi \ r_{y,k}^\psi]^\top$ , and  $[r_{\dot{x},k}^\psi \ r_{\dot{y},k}^\psi]^\top$ , respectively.

The Digital Controller uses  $X_k^\psi$  and  $r_k^\psi$  to generate the input signal  $U_k \triangleq [T_k \ \tau_{x,k} \ \tau_{y,k} \ \tau_{z,k}]^\top$ . Then, a Command Mapping procedure must be performed to obtain the normalized control signals  $\sigma_k \triangleq [\sigma_{k,1} \ \sigma_{k,2} \ \sigma_{k,3} \ \sigma_{k,4}]^\top$  that will be sent as commands to the motors. Inverting the matrix displayed in Eq. (7) and defining  $C_{T_{\text{inv}}} = \frac{1}{4C_T}$ ,  $C_{M_{\text{inv}}} = \frac{1}{4C_M}$  and  $C_{\tau_{\text{inv}}} = \frac{\sqrt{2}}{4dC_T}$ , the squared angular velocities of the motors required to obtain the

forces and torques contained in  $U$  are obtained as follows

$$\begin{bmatrix} \omega_{k,1}^2 \\ \omega_{k,2}^2 \\ \omega_{k,3}^2 \\ \omega_{k,4}^2 \end{bmatrix} = \begin{bmatrix} C_{T_{\text{inv}}} & -C_{\tau_{\text{inv}}} & C_{\tau_{\text{inv}}} & -C_{M_{\text{inv}}} \\ C_{T_{\text{inv}}} & -C_{\tau_{\text{inv}}} & -C_{\tau_{\text{inv}}} & C_{M_{\text{inv}}} \\ C_{T_{\text{inv}}} & C_{\tau_{\text{inv}}} & -C_{\tau_{\text{inv}}} & -C_{M_{\text{inv}}} \\ C_{T_{\text{inv}}} & C_{\tau_{\text{inv}}} & C_{\tau_{\text{inv}}} & C_{M_{\text{inv}}} \end{bmatrix} \begin{bmatrix} T_k \\ \tau_{x,k} \\ \tau_{y,k} \\ \tau_{z,k} \end{bmatrix}. \quad (16)$$

Finally, it follows from (3) that

$$\sigma_{k,i} = \frac{\omega_{k,i} - \omega_b}{C_R}. \quad (17)$$

A zero-order hold is performed on this signal, such that

$$\sigma(t) = \sigma_k, \quad t \in [kT_s, (k+1)T_s]. \quad (18)$$

### 3.1. Digital Controller Structure

All digital controllers implemented in this paper follow the same structure displayed in Fig. 4. The Inner Loop block features controllers that yield the required rolling and pitching moments  $\tau_x$  and  $\tau_y$  to regulate horizontal movement. The Inner Loop block requires the current quadcopter attitude as well as reference signals for roll and pitch to obtain its output, such that

$$\tau_{x,k} = C_{\text{IL},\theta}(\theta_k, \dot{\theta}_k, r_{\theta,k}^i, r_{\dot{\theta},k}^i), \quad (19)$$

$$\tau_{y,k} = C_{\text{IL},\phi}(\phi_k, \dot{\phi}_k, r_{\phi,k}^i, r_{\dot{\phi},k}^i). \quad (20)$$

The reference signals for roll and pitch are obtained from the Outer Loop block, which features controllers that yield the required thrust differential and yawing moments as well as the desired reference signals. Yaw and position are achieved with:

$$\delta T_k = C_{\text{OL},z}(z_k^i, \dot{z}_k^i, r_{z,k}^i, r_{\dot{z},k}^i), \quad (21)$$

$$\tau_{z,k} = C_{\text{OL},\psi}(\psi_k, \dot{\psi}_k, r_{\psi,k}^i, r_{\dot{\psi},k}^i), \quad (22)$$

$$r_{\phi,k}^i = C_{\text{OL},y}(y_k^\psi, \dot{y}_k^\psi, r_{y,k}^\psi, r_{\dot{y},k}^\psi), \quad (23)$$

$$r_{\theta,k}^i = C_{\text{OL},x}(x_k^\psi, \dot{x}_k^\psi, r_{x,k}^\psi, r_{\dot{x},k}^\psi). \quad (24)$$

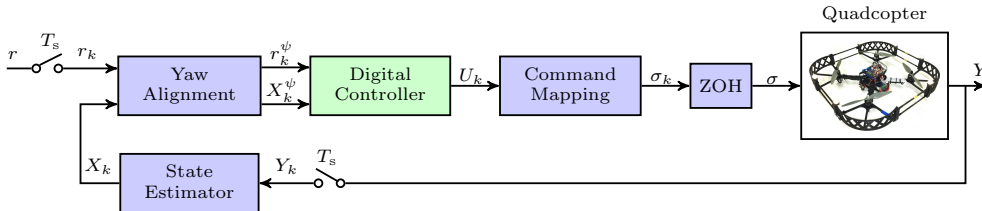


Figure 3: Control system block diagram. The digital controller yields the system input in terms of vertical thrust and torques, which must be mapped into motor commands.

Total thrust is obtained by adding the required thrust differential to hover thrust:

$$T_k = T_{\text{hov}} + \delta T_k. \quad (25)$$

Hence, a set of six control schemes is required for control of the quadcopter. Evaluated control algorithms will be discussed in Section 4. Note that all controllers saturate these signals such that  $\delta T \in [-10.42, 12.34]$  N,  $\tau_x \in [-1.3679, 1.3679]$  N.m,  $\tau_y \in [-1.3679, 1.3679]$  N.m,  $\tau_z \in [-0.1766, 0.1766]$  N.m,  $r_\phi^i \in [-1, 1]$  rad and  $r_\theta^i \in [-1, 1]$  rad. Note that while the saturation limits for  $\delta T$ ,  $\tau_x$ ,  $\tau_y$  and  $\tau_z$  were derived from the thrust and torque limits of the rotors, the saturation limits for  $r_\phi^i$  and  $r_\theta^i$  were chosen arbitrarily to prevent the outer loop controllers from requesting potentially unstable reference signals for roll and pitch.

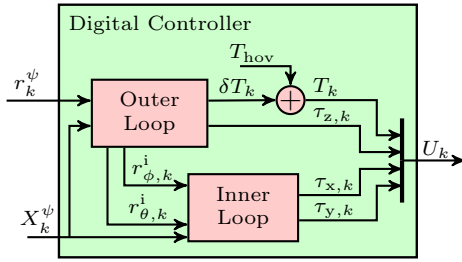


Figure 4: Controller Block Diagram

### 3.2. State Estimation

State feedback controllers require estimates of the full state vector  $X$ . For the quadcopter,  $X \in \mathbb{R}^{12}$  is comprised of three position coordinates ( $x^i, y^i, z^i$ ), three linear velocity components ( $\dot{x}^i, \dot{y}^i, \dot{z}^i$ ), three Euler angles ( $\phi, \theta, \psi$ ), and three angular velocity components ( $\omega_x^b, \omega_y^b, \omega_z^b$ ) per Section 2.2. Position and Euler angle measurements are provided by the MOCAP system. However, the following problems were encountered during experimentation which motivated utilization of a filter:

1. Neither the onboard sensors nor the MOCAP directly provided linear velocity estimates;
2. The yaw estimate from the onboard IMU grew unbounded;
3. Measurements were available asynchronously; the IMU and MOCAP sampling rates were 200 Hz and 100 Hz respectively.

A Kalman Filter (KF) was chosen to filter incoming measurements for several reasons. First, a

KF reduces noise and fuses redundant sensor measurements to provide an estimate  $\hat{X}$  of the entire state vector with the minimum mean-square-error covariance (under linear KF assumptions). Moreover, it can estimate IMU biases thus stopping the unbounded growth of estimates. Finally, a KF can process measurements sequentially as they are sampled, regardless of their sampling rates. In this case, an a priori update is performed every  $T_s$  seconds on all states. If new measurements have been sampled, an a posteriori update is performed as well on all the states with new measurements. These characteristics make the KF an ideal state estimation solution.

Since the linearized dynamics are decoupled, three independent Kalman Filters were designed:

1. Vertical position and velocity ( $z^i, \dot{z}^i$ )
2. Horizontal position and velocity ( $x^i, y^i, \dot{x}^i, \dot{y}^i$ )
3. Yaw and yaw rate ( $\psi, \dot{\psi}$ )

Estimators for pitch, roll, and their respective rates were not required because onboard sensors provided acceptable estimates. In all cases, linear KFs were based on the linearized quadcopter model. The specific Gauss-Markov models for each estimator, as well as their corresponding covariance matrices, are defined in Appendices B, C, and D. Specific calibration values can be found in Appendix E.

### 3.3. State Estimation Performance

Fig. 5 highlights the performance achieved with the proposed state estimation scheme. Note that the top and bottom plots do not share the same

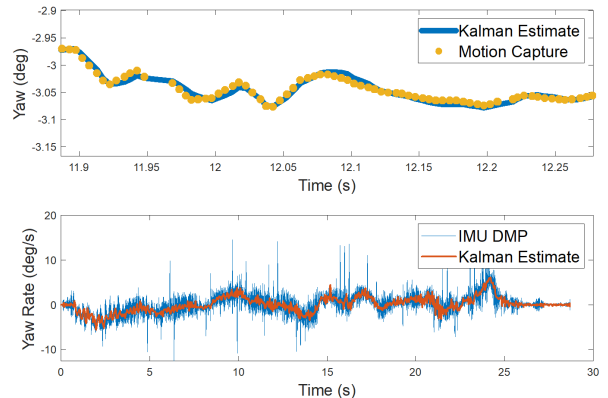


Figure 5: [Top] Yaw vs. time. MOCAP measurements are overlaid on Kalman Filter estimates. [Bottom] Yaw rate vs. time. Kalman Filter estimates are overlaid on IMU DMP measurements.

time scale; the top plot is zoomed in to assist with the following discussion. The top plot shows MOCAP yaw measurements overlaid on the Kalman Filter estimates. Note that, even though MOCAP data was received at a slower rate and at times had gaps in coverage, the Kalman Filter was able to maintain a smooth yaw estimate at all times. This was because the rate gyro (bottom plot) was read at 200 Hz, enabling the estimator to continue propagating both states. Note also that the Kalman yaw rate estimate has less noise than the IMU DMP measurement. These plots demonstrate how fusing measurements sequentially through a Kalman Filter yielded smoother estimates regardless of measurement asynchronicity. Similar performance was achieved with the horizontal and vertical position and velocity estimators.

#### 4. Digital Controllers

This section describes the quadcopter digital control laws along with their tuning procedures using Simulink simulations. A brief summary of requirements and capabilities of the controllers is presented in Table 3. PID and LQR are classical methods well established in the literature (Yun Li et al., 2006; Kwakernaak and Sivan, 1972; Sontag, 1990). MPC is also an established method, though computational overhead challenges implementation on typical real-time embedded computing components found on quadcopters. The proposed quadcopter MPC, LQR, and PID control designs are described below.

Table 3: Controller Comparison

Factors	PID	LQR	MPC
Model required	No	Yes	Yes
Optimization Online	No	No	Yes
Can be made explicit	N/A	N/A	Yes
Implement Constraints	No	No	Yes

##### 4.1. Explicit Model Predictive Control (E-MPC)

Model predictive control (MPC) relies on predicting the response of the system using a model and ensures that the imposed state and control constraints are enforced. At each time step, MPC solves a constrained optimization problem, minimizing a cost function subject to the constraints. The response

of the system is predicted over time period or horizon  $T_h$ . The first move in the optimal control is selected as the control action thereby defining a feedback law (Mayne et al., 2000). The main challenge in using MPC for quadcopters is its high computational cost versus limited onboard computation capabilities. The quadcopter model shown in Section (2.2.4) is nonlinear with 12 states. A direct implementation of MPC to this nonlinear model was not feasible given limited computational resources onboard the quadrotor. Hence, the linearized model around hover (12) is used for prediction. Note that the linearized model decomposes into six submodels (13). For instance, the dynamics of the position state  $\delta x^b$  are described by a double integrator with pitch angle  $\delta\theta$  as an input, whereas the dynamics of pitch angle  $\delta\theta$  are a double integrator with input  $\tau_x$ . Similar considerations apply to the remaining linearized equations. By exploiting this independence, six MPC controllers with small computational footprint can be developed based on the six double integrator models.

Fig. 6 depicts the decoupled MPC control architecture. This figure summarizes the inner and outer loop controller equations introduced in Eqs. (19) – (24). Note that each of the MPC blocks assumes that their respective commanded inputs are applied instantly. However, the propulsion system has internal dynamics that affect generation of  $T, \tau_x, \tau_y$ , and  $\tau_z$ . Similarly, MPC blocks for  $x$  and  $y$  position are designed based on the assumption that pitch and roll angles are achieved instantaneously, yet in fact they have their own dynamics determined by the MPC controllers for  $\theta$  and  $\phi$ . These unmodelled dynamics have not produced substantive constraint violations in the conducted experiments, which justifies the use of this decomposition approach.

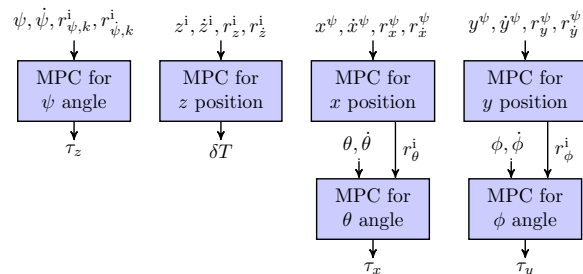


Figure 6: MPC control architecture

As an example, consider MPC design for control

of roll angle (other cases are similar). It follows from (13) that the linearized mode for the dynamics of the roll angle has the form

$$\begin{bmatrix} \delta\dot{\phi} \\ \delta\ddot{\phi} \end{bmatrix} = \begin{bmatrix} 0 & 1 \\ 0 & 0 \end{bmatrix} \begin{bmatrix} \delta\phi \\ \delta\dot{\phi} \end{bmatrix} + \begin{bmatrix} 0 \\ \frac{1}{J_{yy}} \end{bmatrix} \tau_y, \quad (26)$$

where  $\delta\phi = \phi - r_\phi^i$  and  $\delta\dot{\phi} = \dot{\phi}$ . As the states of this system are the deviation with respect to roll setpoint and the roll angular velocity, constraints may be imposed on both of these quantities. In this case, only the roll angular velocity is constrained. It follows from (14) that discretization of (26) with sample time  $T_s$  leads to a discrete-time model of the form

$$\begin{aligned} x_{k+1} &= Ax_k + Bu_k \\ &\equiv \begin{bmatrix} \delta\phi_{k+1} \\ \delta\dot{\phi}_{k+1} \end{bmatrix} = \begin{bmatrix} 1 & T_s \\ 0 & 1 \end{bmatrix} \begin{bmatrix} \delta\phi_k \\ \delta\dot{\phi}_k \end{bmatrix} + \begin{bmatrix} \frac{T_s^2}{2J_{yy}} \\ \frac{T_s}{J_{yy}} \end{bmatrix} \tau_{y,k}. \end{aligned} \quad (27)$$

The roll angle MPC controller uses (27) as the prediction model and determines control action based on solving the following finite-horizon discrete-time optimal control problem:

$$\begin{aligned} \min_{u_0, u_1, \dots, u_{N-1}} \quad & x_N^T P x_N + \sum_{k=0}^{N-1} x_k^T Q x_k + u_k^T R u_k \\ \text{s.t.} \quad & x_{k+1} = Ax_k + Bu_k, \\ & x_0 \text{ is the current state,} \\ & |\dot{\phi}_k| \leq \dot{\phi}_{\max}, \end{aligned} \quad (28)$$

where  $N = T_h/T_s$ ,  $Q, R$  are positive definite matrices and  $P$  is given by the solution of the discrete time algebraic Riccati equation in the infinite horizon version of (28) without control constraints. The MPC feedback law is  $u_{\text{MPC},x} = u_0$ . This MPC formulation recovers the solution of the associated LQR problem when constraints remain inactive.

As is stated in Cairano and Bemporad (2009), the optimization problem (28) can be written in condensed form as

$$\begin{aligned} \min_U \quad & \frac{1}{2} U^T H U + q^T U \\ \text{s.t.} \quad & G U \leq W, \end{aligned} \quad (29)$$

where  $U = (u_0, u_1, \dots, u_{N-1})^T$  and  $H, q, G, U$  are matrices that depend on  $A, B, x_0$  and the constraints of the system.

Solving the optimization problem as stated in Eq. (29) in real time on a Beaglebone Blue using a standard dual projection gradient algorithm implemented in C has proven to be challenging. For instance, with the prediction horizon set to 1 s to capture all transients and a sampling period  $T_s$  equal to 20 ms, around 100 ms was needed to solve the optimization problem (29). Note that this time may be reduced with advanced time-distributed optimization strategies as described in Liao-McPherson et al. (2020), although the problem of reducing the computation time remains difficult.

Therefore, an explicit MPC (E-MPC) approach was pursued. With E-MPC, each problem (29) is parameterized by initial condition  $x_0$  which is a two dimensional vector. The solution to problem (29) can be precomputed offline and the resulting control values can be stored in a two dimensional lookup table for online use in the Beaglebone processor. To address the potential infeasibility of problem (29), which can occur due to large disturbances, as was observed during flight tests, the implemented algorithm switches to an unconstrained LQR under such circumstances.

The particular structure of the quadcopter system dynamics and constraints is critical for the proposed implementation of E-MPC. When the system is linearized about a hovering condition, six two-dimensional smaller subsystems are obtained. These systems are not coupled, i.e., the control input computation is unidirectional, so there is no feedback between the six smaller subsystems (see Figure 6). Furthermore, the constraints on the system can be independently enforced on these smaller subsystems, i.e., there are no constraints that combine states/inputs of different subsystems. This convenient combination of decoupled dynamics and independent constraints is what allows the computation and storage of the control inputs as six two-dimensional look-up tables. Note that if the dimension of the smaller subsystems increases, then the size of the solution look-up table of (29) grows exponentially. Hence, E-MPC may quickly become intractable for more complex problems. Our approach can be viewed as an instantiation of a more general idea of exploring symmetries in E-MPC design, see e.g., Danielson and Borrelli (2015).

To tune MPC controller parameters, the sampling frequency was set to 200 Hz, sufficiently fast for stability. To capture transients, time horizon was set to 1 s. Constraints were set to illustrate MPC's constraint handling capability. Matrices  $Q$

Table 4: Parameters of the six Model Predictive Controllers

Parameter	$x$	$y$	$z$	$\theta$	$\phi$	$\psi$
$F_s$	200 Hz	200 Hz	200 Hz	200 Hz	200 Hz	200 Hz
$T_h$	1 s	1 s	1 s	1 s	1 s	1 s
$ x_{\max} $	1000 m	1000 m	1000 m	1000 rad	1000 rad	1000 rad
$ \dot{x}_{\max} $	5 m/s	5 m/s	5 m/s	45 deg/s	45 deg/s	90 deg/s
$ u_{\max} $	45 deg	45 deg	1000 N	1000 N.m	1000 N.m	1000 N.m
$Q$	diag([150, 200])	diag([150, 200])	diag([490, 117])	diag([5, 1.5])	diag([5, 1.5])	diag([100, 15])
$R$	5000	5000	5.5	10	10	1000

and  $R$  were chosen by trial and error during outdoor tests. The parameters of each of six MPC controllers are summarized in Table 4.

#### 4.2. Discrete LQR and LQR-I Control

Discrete-time LQR exploits a linear discrete-time model  $x_{k+1} = Ax_k + Bu_k$ , and generates the control sequence according to  $u_k = -Kx_k$ , where  $K = (R + B^T P B)^{-1} B^T P A$ , to minimize performance index

$$J = \sum_{k=0}^{\infty} x_k^T Q x_k + u_k^T R u_k.$$

In this expression,  $P$  is the unique positive semi-definite solution to the discrete Algebraic Riccati Equation.

The design of the LQR and LQR-I controllers for each of the six subsystems is based on their models (14). Thus, the overall LQR design is decoupled into six controllers similar to the MPC design. Hence, in the LQR case, the controller has the form

$$\begin{aligned} \delta U_k &= \text{LQR}_{\mathbb{X}}(\mathbb{X}_k, \dot{\mathbb{X}}_k, r_{\mathbb{X},k}, r_{\dot{\mathbb{X}},k}) \\ &= [K_{\mathbb{X}} \quad K_{\dot{\mathbb{X}}}] \cdot \begin{bmatrix} r_{\mathbb{X},k} - \mathbb{X}_k \\ r_{\dot{\mathbb{X}},k} - \dot{\mathbb{X}}_k \end{bmatrix} = [K_{\mathbb{X}} \quad K_{\dot{\mathbb{X}}}] \cdot \begin{bmatrix} \delta \mathbb{X}_k \\ \delta \dot{\mathbb{X}}_k \end{bmatrix}, \end{aligned} \quad (30)$$

where  $K_{\mathbb{X}}$  and  $K_{\dot{\mathbb{X}}}$  are LQR gains,  $\mathbb{X}$  is the state,  $\dot{\mathbb{X}}$  is its time derivative and  $r_{\mathbb{X},k}, r_{\dot{\mathbb{X}},k}$  are setpoints which are consistent with the unforced dynamics of (14). The state and control weighting matrices  $Q_{\mathbb{X}}$  and  $R_{\mathbb{X}}$  are used as tuning parameters.

In the LQR-I case, the controller is based on the augmented model using (14) with integrator state  $\mathbb{X}_{\text{int}}$ , which has the form

$$\begin{aligned} \begin{bmatrix} \delta \mathbb{X}_{k+1} \\ \delta \dot{\mathbb{X}}_{k+1} \\ \mathbb{X}_{\text{int},k+1} \end{bmatrix} &= \begin{bmatrix} 1 & T_s & 0 \\ 0 & 1 & 0 \\ T_s & 0 & 1 \end{bmatrix} \begin{bmatrix} \delta \mathbb{X}_k \\ \delta \dot{\mathbb{X}}_k \\ \mathbb{X}_{\text{int},k} \end{bmatrix} + \begin{bmatrix} B T_s \\ 0 \end{bmatrix} \delta U_k \\ &= A_{\mathbb{X},\text{int}} \begin{bmatrix} \delta \mathbb{X}_k \\ \delta \dot{\mathbb{X}}_k \\ \mathbb{X}_{\text{int},k} \end{bmatrix} + B_{\mathbb{X},\text{int}} \delta U_k \end{aligned} \quad (31)$$

Hence, the optimal gains  $K_{\mathbb{X}}$ ,  $K_{\dot{\mathbb{X}}}$  and  $K_{\mathbb{X},\text{int}}$  are obtained by solving the discrete Algebraic Riccati Equation using  $A_{\mathbb{X},\text{int}}$ ,  $B_{\mathbb{X},\text{int}}$ ,  $Q_{\mathbb{X},\text{int}}$  and  $R_{\mathbb{X},\text{int}}$ . The LQR-I controller is augmented with anti-windup (see Fig. 7). Note that the integrator is placed right before the output so that the limit established by the anti-windup is placed on the controller output rather than on the integrator state. The output  $u_k$  is saturated and can only take a maximum value of  $u_{\max}$  and a minimum value of  $u_{\min}$ , while the rate at which the integrator “winds-down” depends on gain  $\tau_{\text{int}}$ . LQR-I anti-windup can be written as

$$\delta U_k = \text{LQR}_{x,\text{AW-Int}}(\mathbb{X}_k, \dot{\mathbb{X}}_k, r_{\mathbb{X},k}, r_{\dot{\mathbb{X}},k}) \quad (32)$$

Note that outputs obtained from traditional LQR control are also subject to output saturation.

A cascaded LQR/LQR-I controller scheme is employed in the quadcopter. Fig. 8 shows the chosen architecture for these controllers. Roll and pitch are regulated by LQR controllers since they simplify the design of the cascaded LQR-I controllers and to prevent overshoot inherent to integrators in roll and pitch. LQR controllers are tuned from the values assigned to  $Q$  and  $R$  matrices. Usually, only the diagonal terms of these matrices are given nonzero values. Higher values in the diagonal of the  $Q$  matrix yield a more aggressive behavior when tracking the states associated with each value, while higher values in the diagonal of the  $R$  matrix yield a more conservative behavior when tracking the states associated with the respective input. Parameters selected for the LQR and LQR-I controllers are summarized in Table 5.

#### 4.3. PID and PD Controllers

The PID controller in continuous-time has the following form:

$$u(t) = K_p e(t) + K_i \int_0^t e(\tau) d\tau + K_d \frac{de(t)}{dt} \quad (33)$$

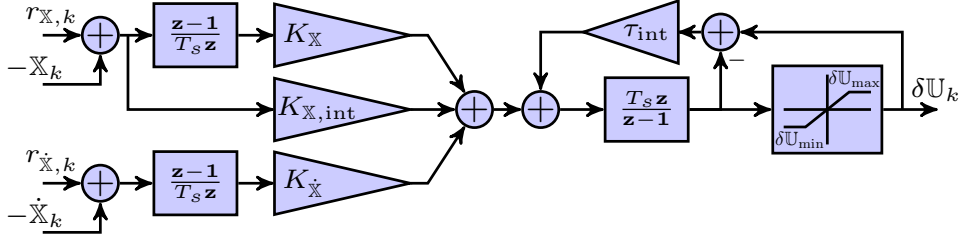


Figure 7: Block diagram of LQR-I controller scheme with integrator anti-windup, where  $\mathbf{z}$  is the Z-transform variable.

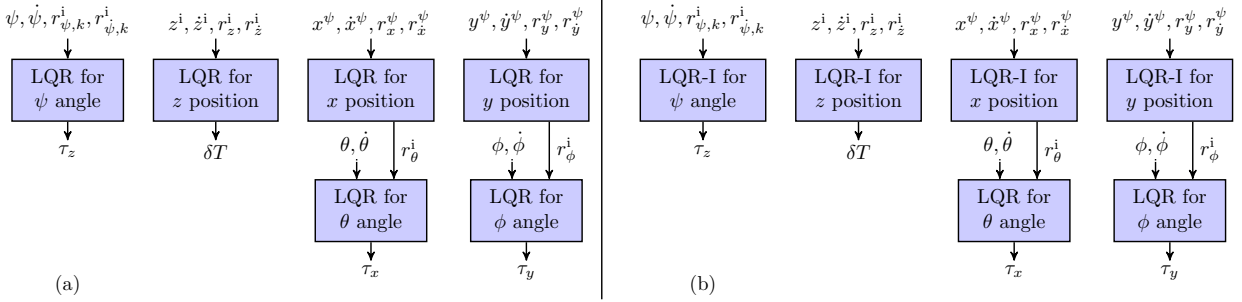


Figure 8: Control architecture for the LQR (a) and LQR-I (b) controllers.

Table 5: Parameters of the six LQR ( $Q = \text{diag}([Q_p, Q_d])$ ) and LQR-I ( $Q = \text{diag}([Q_p, Q_d, Q_i])$ ) Controllers

Parameter	LQR						LQR-I					
	$x$	$y$	$z$	$\theta$	$\phi$	$\psi$	$x$	$y$	$z$	$\theta$	$\phi$	$\psi$
$Q_p$	85	85	2000	5.06	5.06	7	50	50	490	5	5	1
$Q_d$	100	100	100	1.55	1.55	0.25	195	195	117	1.5	1.5	15
$Q_i$	—	—	—	—	—	—	25	25	12.6	—	—	10
$R$	515	515	4	4	4	875	1000	1000	5.5	10	10	1000

where  $e$  denotes the tracking error,  $u$  is the control signal,  $K_p$ ,  $K_i$  and  $K_d$  are the controller gains. Such a controller is implemented in discrete-time on the quadcopter using a Z-transform formulation:

$$C(\mathbf{z}) = K_p + K_i \frac{T_s}{\mathbf{z} - 1} + K_d \frac{N}{1 + NT_s/(\mathbf{z} - 1)}, \quad (34)$$

where typical values of  $N$  range from 8 to 20, and  $\mathbf{z}$  is the Z-transform variable. Note that the derivative term in Eq. (34) is combined with a low pass filter to mitigate sensitivity of the derivative action to measurement noise (Åström and Hägglund, 1995). Furthermore, note that the PID controller given by Eq. (34) does not include an anti-windup mechanism, unlike the integral term in the proposed LQR-I scheme. We have chosen such a controller as a benchmark for comparison because PID controllers without anti-windup are commonly offered as commercial-off-the-shelf solutions, e.g., in

our case we used the PID function already provided in the Robot Control Library, which consists of a C code implementation of Eq. (34).

A cascaded PID/PD controller scheme is employed in the quadcopter. Fig. 9 shows the chosen architecture for these controllers. First, the desired roll, desired pitch, and thrust are determined based on position error. Then, required torques are calculated based on desired attitude. Note that the controllers for roll and pitch are PD controllers since they simplify the design of the cascaded PID controllers and prevent undesired overshoot, similar to the cascaded LQR design above. Parameters for the PD and PID controllers are summarized in Tables 6 and 7. Note that, while the discrete PD and PID structures are the same in the simulation as in the embedded implementation, the parameters used for the simulations and for the experiments are dif-

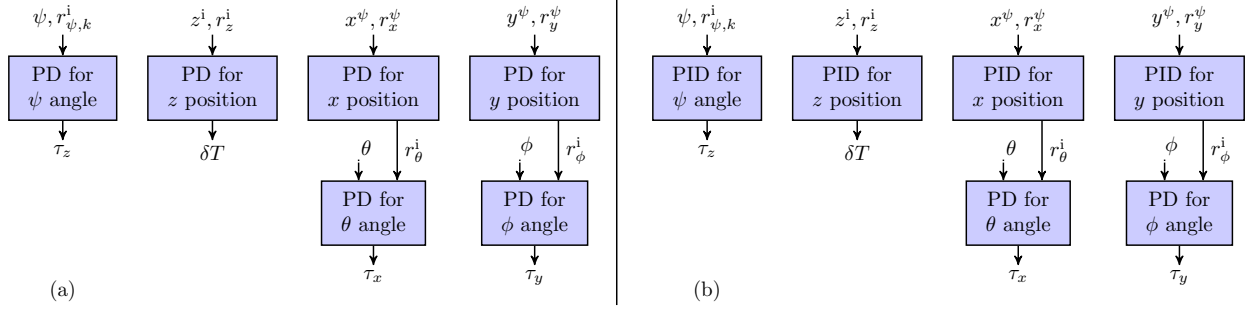


Figure 9: Control architecture for PD (a) and PID (b) controllers.

Table 6: Parameters of the Six PD Controllers

Parameter	Simulation						Experiment					
	$x$	$y$	$z$	$\theta$	$\phi$	$\psi$	$x$	$y$	$z$	$\theta$	$\phi$	$\psi$
$K_p$	0.6	0.6	5	0.25	0.25	0.1	0.5	0.5	8	0.75	0.75	1.5
$K_d$	0.135	0.135	3.5	0.225	0.225	0.075	0.05	0.05	3.5	0.2	0.2	0.1
$N$	62.83	62.83	62.83	62.83	62.83	31.41	62.83	62.83	62.83	62.83	62.83	31.41

Table 7: Parameters of the six PID Controllers

Parameter	Simulation						Experiment					
	$x$	$y$	$z$	$\theta$	$\phi$	$\psi$	$x$	$y$	$z$	$\theta$	$\phi$	$\psi$
$K_p$	0.6	0.6	5	0.25	0.25	0.1	0.5	0.5	5	0.75	0.75	1.5
$K_i$	0.15	0.15	1	–	–	0.025	0.15	0.15	1	–	–	0.5
$K_d$	0.135	0.135	3.5	0.225	0.225	0.075	0.05	0.05	3.5	0.2	0.2	0.1
$N$	62.83	62.83	62.83	62.83	62.83	31.41	62.83	62.83	62.83	62.83	62.83	31.41

ferent since the simulation parameters yielded an unstable behavior during the tests.

## 5. Quadcopter Simulation

The block diagram of a closed loop simulation model implemented in Simulink is shown in Fig. 10. The Motor Dynamics block simulates the dynamics of each of the four motors/propulsors used by the quadcopter, represented by Eqs. (3) - (7). The inputs of this block are the PWM signals  $\sigma$  and its output is the quadcopter dynamic system input vector  $U$ . The Quadcopter Dynamics block simulates the dynamics represented by Eqs. (9) - (11). The input of this block is the input vector  $U$  and its output is the current state vector  $X$ . The Yaw Alignment block transforms the reference setpoint vector  $r_k$  and the state vector  $X_k$  into  $r_k^\psi$  and  $X_k^\psi$ , as stated in (15). The Digital Controller block contains the inner and outer loop controllers per Section 3.1 and yields the discrete quadcopter system vector input vector  $U_k$ . Finally, the Command

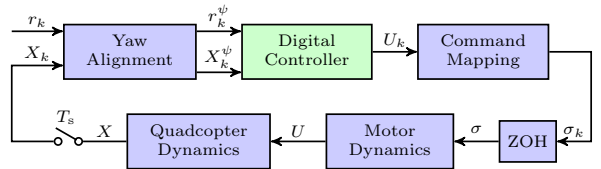


Figure 10: Simulink Model Block Diagram. The blocks are arranged such that the dynamics models run in continuous time while the controller does so at given time intervals.

Mapping block obtains  $\sigma_k$  from  $U_k$  per Eqs. (16) and (17). The ZOH block holds  $\sigma_k$  for  $T_s$  seconds, thus converting this discrete signal into the continuous signal  $\sigma_k$ , as described in Eq. (18).

Figs. 11, 12, 13, 14, and 15 show simulation results using step reference setpoint signals for  $r_x^i$ ,  $r_y^i$ ,  $r_z^i$  and  $r_\psi^i$  for the PD, PID, LQR, LQR-I and MPC controllers, respectively. In the next section, simulation results using an inclined, circular trajectory are compared against experimental results to evaluate performance.

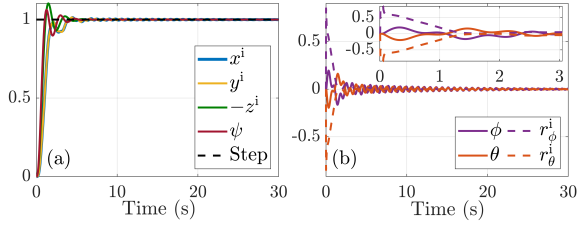


Figure 11: Simulation results for PD controller. (a) shows the response to a unit step in the position setpoint in the x-axis direction, in the y-axis direction, in the negative z-axis direction and in the positive direction of  $\psi$ . (b) shows the setpoint signals and trajectories of  $\phi$  and  $\theta$  in response to a unit step in the position setpoint in the y-axis direction and in the x-axis direction, respectively.

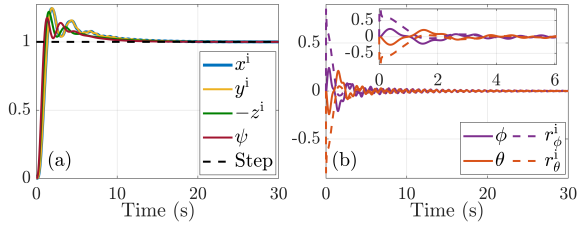


Figure 12: Simulation results for PID controller. (a) shows the response to a unit step in the position setpoint in the x-axis direction, in the y-axis direction, in the negative z-axis direction and in the positive direction of  $\psi$ . (b) shows the setpoint signals and trajectories of  $\phi$  and  $\theta$  in response to a unit step in the position setpoint in the y-axis direction and in the x-axis direction, respectively.

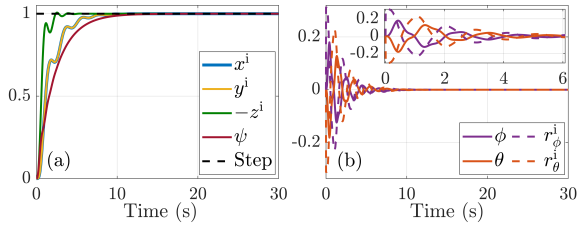


Figure 13: Simulation results for LQR controller. (a) shows the response to a unit step in the position setpoint in the x-axis direction, in the y-axis direction, in the negative z-axis direction and in the positive direction of  $\psi$ . (b) shows the setpoint signals and trajectories of  $\phi$  and  $\theta$  in response to a unit step in the position setpoint in the y-axis direction and in the x-axis direction, respectively.

## 6. Experimental Setup

The quadcopter outdoor flight test architecture is shown in Fig. 16. The attitude and position information of the quadcopter is obtained from the MOCAP system. This MOCAP data is serially transmitted to a Beaglebone Green (BBG), which then wirelessly relays it to the quadcopter using an XBee

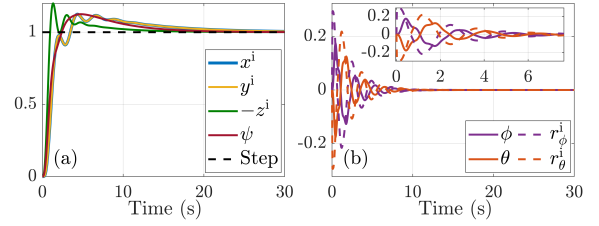


Figure 14: Simulation results for LQR-I controller. (a) shows the response to a unit step in the position setpoint in the x-axis direction, in the y-axis direction, in the negative z-axis direction and in the positive direction of  $\psi$ . (b) shows the setpoint signals and trajectories of  $\phi$  and  $\theta$  in response to a unit step in the position setpoint in the y-axis direction and in the x-axis direction, respectively.

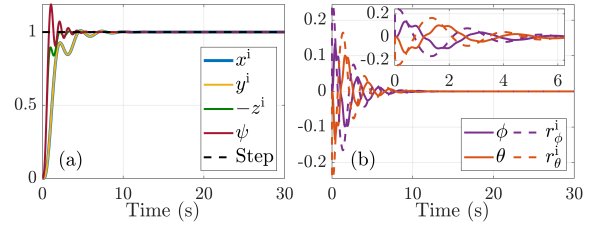


Figure 15: Simulation results for MPC controller. (a) shows the response to a unit step in the position setpoint in the x-axis direction, in the y-axis direction, in the negative z-axis direction and in the yaw angle in the positive direction of  $\psi$ . (b) shows the setpoint signals and trajectories of  $\phi$  and  $\theta$  in response to a unit step in the position setpoint in the y-axis direction and in the x-axis direction, respectively.

radio modem. The MOCAP data is then fused by the Kalman Filter (described in Section 3.2) to produce a state estimate.

To mitigate the impact of short-term MOCAP data dropouts (due to varying lighting conditions, changes in ambient temperature, etc.), the Kalman Filter provided state estimates based solely on on-board sensor data. Also, a digital wind vane was used to measure wind during outdoor flight tests.

In the experiments reported in this paper, the quadcopter tracked an inclined, circular trajectory while continuously changing its heading angle, as shown in Fig. 17. For the circular section of the trajectory, the quadcopter followed a trapezoidal velocity profile. For the straight sections, it followed a cubic velocity profile. All controllers were flown at tangential velocities of 1, 2, 3, and 4 m/s (three times each) along a circle of radius 4.5 m, inclined at an angle of  $-7.5$  deg along the y-axis.

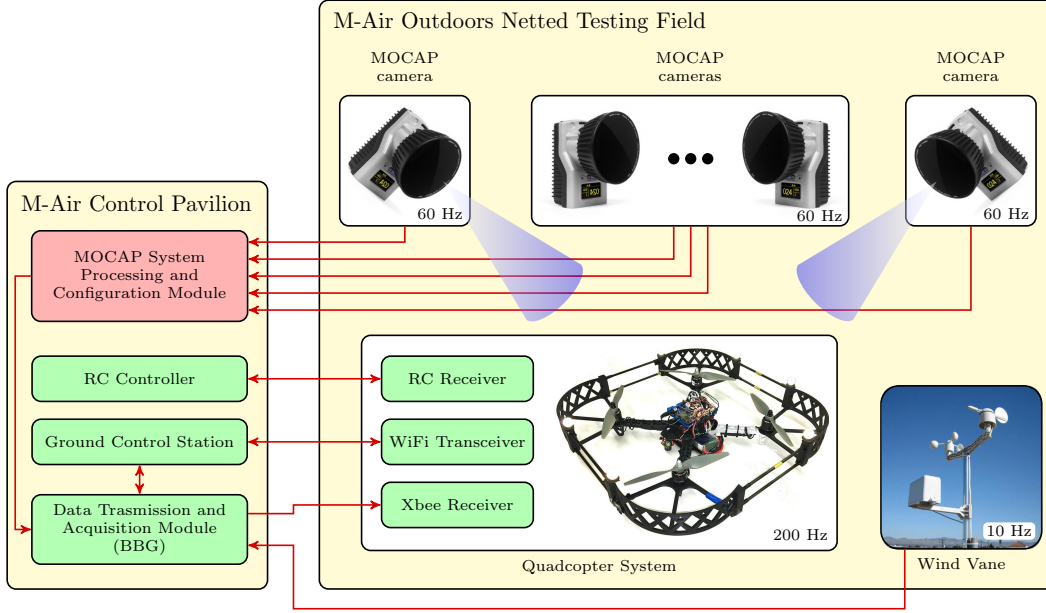


Figure 16: Quadcopter Flight Test Architecture.

## 7. Results

In this section, step responses, position and velocity tracking errors of an inclined circle, and control effort plots are presented. Each controller was manually tuned to achieve the best performance.

Figs. 18 – 22 compare simulation and experimental results for a tangential velocity of 2 m/s. Note that the noise in the velocity estimates from the experimental data was due to the Kalman Filter propagation of noisy sensor measurements.

Experimental results from inclined, circular trajectory tracking in M-Air over all the tangential velocities are summarized in Table 8. It is apparent that integral action reduces of maximum radial and altitude error. Negligible wind was present.

Table 8: Position tracking performance of quadcopter controllers over all experiments

Controller	Avg. Tracking Error (m)	Max Tracking Error	
		Radial(m)	Altitude(m)
PD	0.5373	1.408	0.4507
PID	0.1722	0.53462	0.2348
LQR	0.4450	1.1852	0.3854
LQR-I	0.3470	1.027	0.628
E-MPC	0.9292	1.7404	0.708

Fig. 23 provides controller performance details at different tangential velocities. The position and

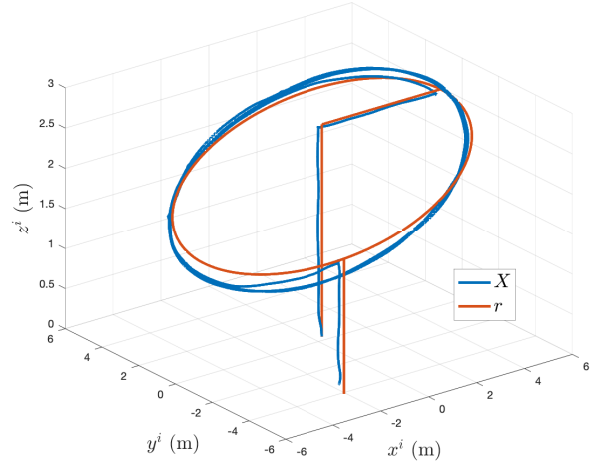


Figure 17: 3D plot illustrating the inclined, circular reference trajectory and tracking results of the quadcopter LQR controller. For ease of viewing, the coordinates are North-West-Up in this plot.

velocity errors are calculated by taking the norm of the error vector. It can be seen that an increase in tangential velocity along the circle led to an increase in position and velocity error.

The control effort of each controller was calculated using the following formula:

$$\text{Control Effort} = \frac{\|u\|_2}{T_{\text{total}}}, \quad (35)$$

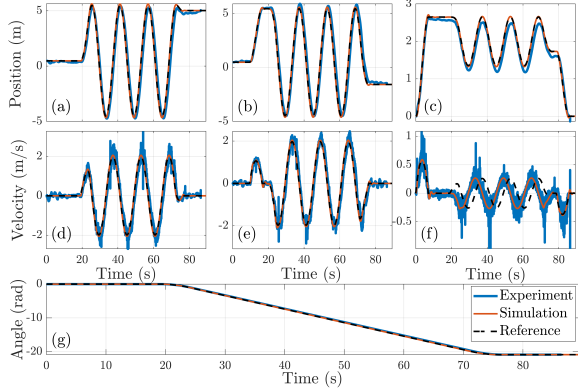


Figure 18: Experimental results (exp subscript) versus simulation results (sim subscript) for PD controller for a tangential velocity of 2 m/s. (a) x-axis position. (b) y-axis position. (c)  $-z$ -axis position. (d) x-axis velocity. (e) y-axis velocity. (f)  $-z$ -axis velocity. (g) Yaw.

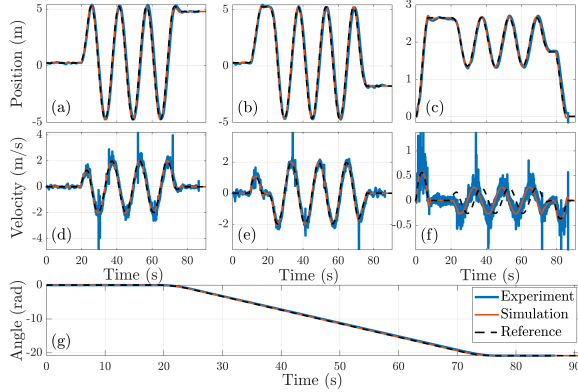


Figure 19: Experimental results (exp subscript) versus simulation results (sim subscript) for PID controller for a tangential velocity of 2 m/s. (a) x-axis position. (b) y-axis position. (c)  $-z$ -axis position. (d) x-axis velocity. (e) y-axis velocity. (f)  $-z$ -axis velocity. (g) Yaw.

where  $u$  is the control input to the motors and  $T_{\text{total}}$  is the total time to execute the circular trajectory.

Control effort is presented in Fig. 24. Nearly all the controllers had similar control effort. However, a significant change in control effort was observed with a change in operating temperatures.

The E-MPC control scheme offers the capability to handle state constraints. In the conducted experiments, roll rate and pitch rate constraints were imposed to restrict aggressive attitude changes that might destabilize the system. It can be seen in Figs. 25 and 26 that E-MPC satisfies a maximum 45 deg/s magnitude rate constraint for a tangential velocity of 4 m/s. In the the case of the other control schemes, constraints were violated as

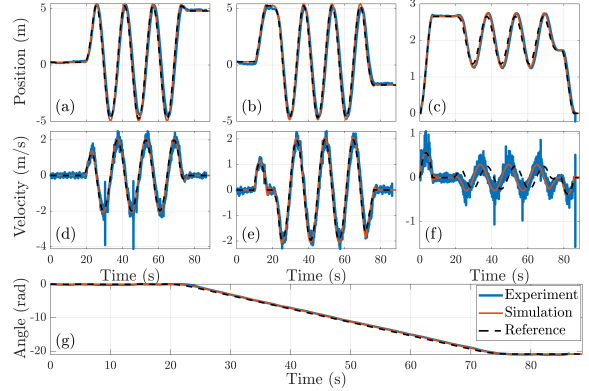


Figure 20: Experimental results (exp subscript) versus simulation results (sim subscript) for LQR controller for a tangential velocity of 2 m/s. (a) x-axis position. (b) y-axis position. (c)  $-z$ -axis position. (d) x-axis velocity. (e) y-axis velocity. (f)  $-z$ -axis velocity. (g) Yaw.

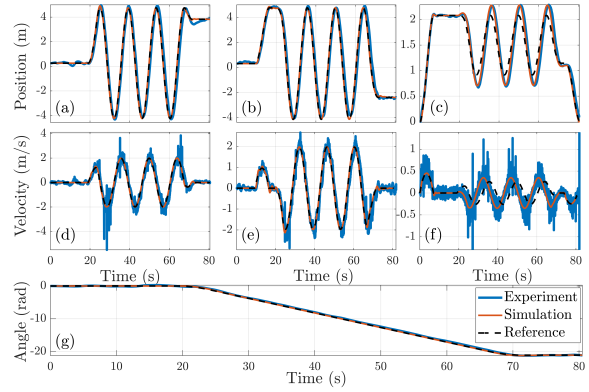


Figure 21: Experimental results (exp subscript) versus simulation results (sim subscript) for LQR-I controller for a tangential velocity of 2 m/s. (a) x-axis position. (b) y-axis position. (c)  $-z$ -axis position. (d) x-axis velocity. (e) y-axis velocity. (f)  $-z$ -axis velocity. (g) Yaw.

there was no mechanism to enforce them. Example results presented here are for one flight; however, similar outcomes were observed in the other experiments. The benefits of constraint satisfaction could only be observed at higher velocities since, at lower velocities, the rates were within limits for all controllers. Reference trajectories with a tangential velocity of 5 m/s could only be completed when using the E-MPC controller. When the other control schemes (PD, PID, LQR and LQR-I) were used, the higher speeds required for trajectory tracking resulted in crashes when moving downwards due to the increased momentum, which E-MPC managed to constrain. This pattern suggests that detuning the gains of the other control schemes to

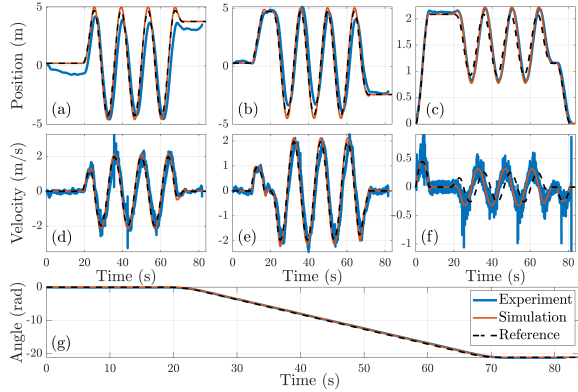


Figure 22: Experimental results (exp subscript) versus simulation results (sim subscript) for MPC controller for a tangential velocity of 2 m/s. (a) x-axis position. (b) y-axis position. (c)  $-z$ -axis position. (d) x-axis velocity. (e) y-axis velocity. (f)  $-z$ -axis velocity. (g) Yaw.

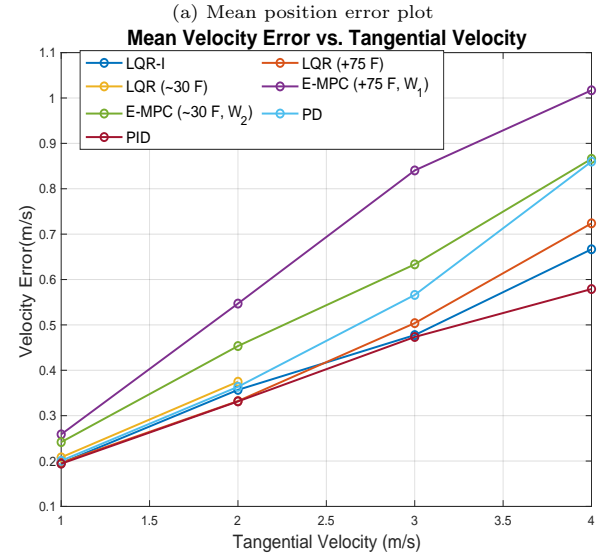
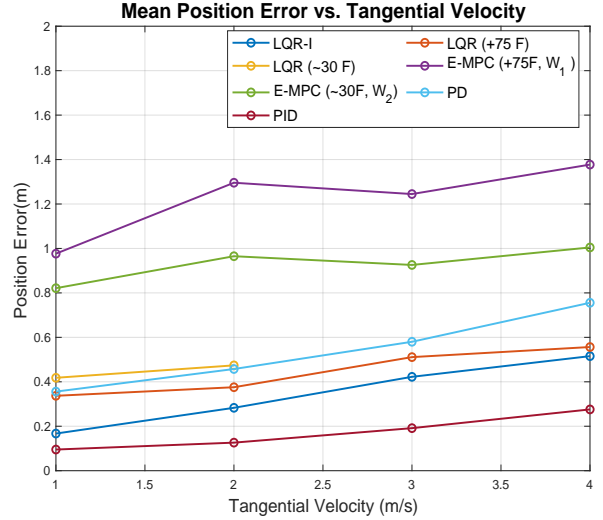
slow down the translational response could have prevented the crashes at the expense of tracking performance; however, that study is left for future work.

### 7.1. Data Playback for Controller Timing Analysis

In order to benchmark onboard controller computation times, experimental data was played back using the Beaglebone Blue on a benchtop. In these simulations, only the controllers were executed to determine the amount of time required to generate a control command in each loop. The results from the data playback simulations are presented in Table 9. It was observed that, on average, the LQR controller took the least amount of time to compute the control command while E-MPC took the most. Note that the mean computation times of all controllers were less than the time between system interrupts ( $T_s = 5000 \mu s$ ) and that only the worst case computations times of PID and LQR-I exceeded this time.

Table 9: Controller computation time from data playback

Controller	Computation Time ( $\mu s$ )		Worst Case ( $\mu s$ )
	Mean	$\sigma$	
LQR	5.2468	3.0878	314
LQR-I	6.7263	35.0383	8163
PD	8.8461	7.6955	1424
PID	9.3786	29.3469	5071
E-MPC	13.6239	6.6481	1301



(a) Mean position error plot

(b) Mean velocity error plot

Figure 23: Results from outdoor quadcopter experiments, with different ambient temperatures for LQR and E-MPC.

## 8. Discussion

Fig. 23 shows that, out of all controllers, the implemented PID controller had the best tracking performance. However, while the same controller parameters were used in both the simulations and experiments for the LQR, LQR-I, and MPC cases, different parameter sets were required for the PD and PID simulations and experiments (as was explained in Section 4.3). Hence, it can be argued that LQR-I offered a better compromise between tracking performance and maintaining consistent

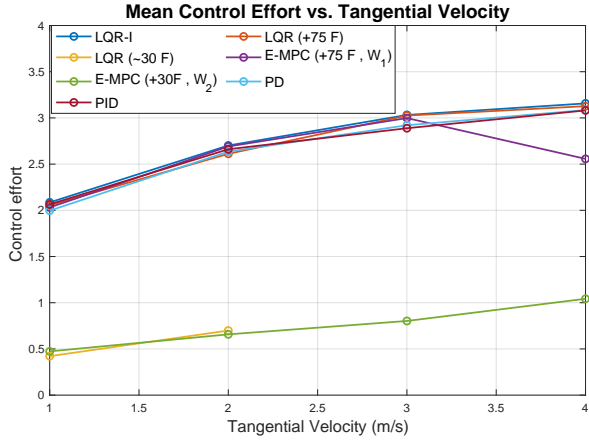


Figure 24: Control effort plot for quadcopter tracking an inclined circle, with different ambient temperatures for LQR and E-MPC.

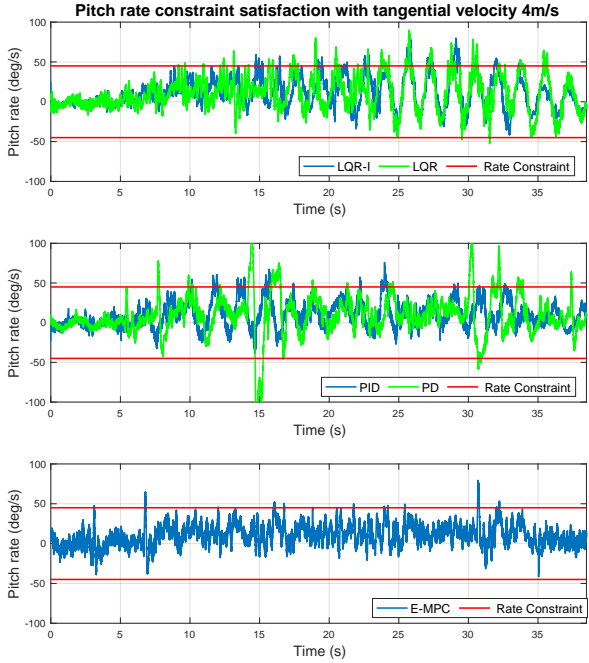


Figure 25: Pitch rate constraint satisfaction supported by E-MPC compared to other control schemes, while executing an inclined circle with tangential velocity of 4 m/s

simulation and experimental performance.

With an increase in tangential velocity, an increase in position and velocity error was observed. This can be attributed to the inertia of the vehicle which resists changes in attitude and position, especially at higher velocities. Furthermore, due to their low KV, the motors lacked the control authority to rapidly change quadcopter attitude. However, an

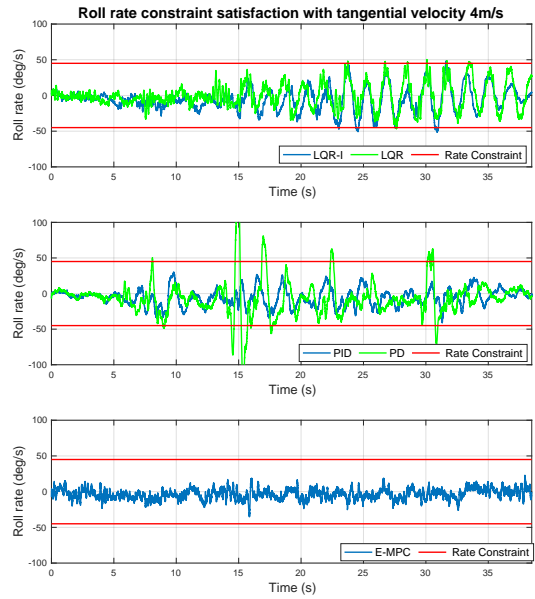


Figure 26: This plot illustrates the roll rate constraint satisfaction capability of E-MPC compared to other control schemes, while executing an inclined circle with tangential velocity of 4m/s

increase in motor KV may require different battery characteristics, which may increase the weight and require a different set of propellers. Hence, an appropriate combination of motors and propellers is required for satisfactory flight performance.

Fig. 24 shows insignificant control effort variation across controllers under similar flight conditions. However, lower ambient temperatures reduced the required control effort. This can be attributed to the higher density of freezing air ( $-1\text{ }^{\circ}\text{C}$  during the experiments), which required lower control effort to propel the quadcopter. Similar results were presented in Paredes et al. (2017), where more energy was consumed at higher altitudes with lower air density while less energy was consumed at lower altitudes with higher air density (for similar flight times).

Fig. 25 shows E-MPC controller constraint violations at approximately 7 s and 31 s. These spikes were attributed to random delays in MOCAP information, thus acting as noise for the system. Overall, the E-MPC scheme proved helpful in situations where aggressive trajectory tracking was required while satisfying constraints.

The data playback simulations showed that, on average, LQR took the least amount of time to compute control commands while E-MPC took the

most. This was due to the fact that E-MPC determines gains based on a lookup table as opposed to other controllers which use predefined gains. These simulations also showed that the mean computation times of all controllers were less than the time between system interrupts ( $T_s = 5000 \mu s$ ) and that only the worst case computation times of PID and LQR-I exceeded this time. This implies that all controllers will usually meet the time constraint imposed by the embedded system. Furthermore, since the PID and LQR-I controllers had the best tracking performance and completed all test flights, it can be inferred that the cases where these don't meet the time constraint are rare and don't have a significant impact on tracking performance. Since the only controllers that exceeded the time constraint feature an integrator, improving the computational efficiency of the algorithm that implements the integrator might decrease the probability of time constraint violation.

## 9. Conclusions

This paper reviews quadrotor system modeling, state estimation, and control. Multiple digital controllers were successfully designed based on a linearized quadcopter model and were implemented on a computationally limited embedded platform. Tested controllers included PD, PID, LQR, LQR-I, and E-MPC. These controllers were evaluated in the M-Air outdoor motion capture facility during inclined, circular flight sequences. Various challenges such as limited onboard computational power and loss of MOCAP tracking during outdoor flight were encountered with mitigation methods provided. Reported results for E-MPC, LQR, LQR-I, PD, and PID controllers analyzed position tracking error, velocity tracking error, and control effort. Overall, PID had the best tracking performance, LQR-I offered a better compromise between tracking performance and maintaining consistent simulation and experimental performance, and LQR had the fastest average computation time. All controllers satisfied the time constraint imposed by the embedded system.

If constraints must be met on a computationally limited platform, E-MPC provides an effective solution by computing gains offline and using a lookup table in-flight. However, E-MPC must rely on a backup (e.g., LQR) when conditions stray from precomputed cases. Controller selection should be based on factors such as available computational

power, mission specifications (e.g. velocity constraints), and a designer's ability to determine optimal gains and performance. Appropriate motor and propeller selection is also a key element in quadcopter design. For example, trajectories requiring aggressive velocities or quick changes in direction need higher KV motors.

Note that, other than PID, most of the control approaches discussed in this paper require modelling information. "Model-free" approaches to quadcopter control have been proposed and successfully implemented, as shown in Al Younes et al. (2016); Bekcheva et al. (2018) for example, where an ultra-local model is estimated online and used to compensate for uncertainties and disturbances. The comparison with such model-free approaches is left as a subject for future research.

The authors hope this paper will serve as a comprehensive guide for engineers needing to select, design, implement, and tune a quadcopter digital control solution.

## Appendix

### A. Propulsion Modeling

The thrust  $T$  (in N) and torque  $M$  (in  $N \cdot m$ ) generated by a propeller spinning at  $\omega$  RPM are given by,

$$T = C_T \omega^2, \quad (36)$$

$$M = C_M \omega^2, \quad (37)$$

where  $C_T$  and  $C_M$  are computed through a least squares fit on the RPM versus Thrust and RPM versus Moment curves shown in Fig. 27. The R-squared value of the fit for  $C_T$  was 0.9983, whereas the R-squared value for  $C_M$  was 0.9988. These high R-squared values show that the fits were very accurate. The motors were driven by a normalized control signal  $\sigma$  that goes from 0 (motor not spinning) to 1 (full throttle). The steady state angular velocity of the propeller  $\omega$  (in RPM) is fit with a linear model with respect to  $\sigma$ ,

$$w_{ss} = C_R \sigma + \omega_b, \quad (38)$$

where  $C_R$  and  $\omega_b$  were obtained with a least squares fit on the curve  $\sigma$  versus RPM curve shown in Fig. 27. The R-squared value of this fit was 0.9911, showing that the linear model fit the experimental data accurately. It is interesting to note that the fit was worse for  $\sigma < 0.2$  and  $\sigma \approx 1$  due to the

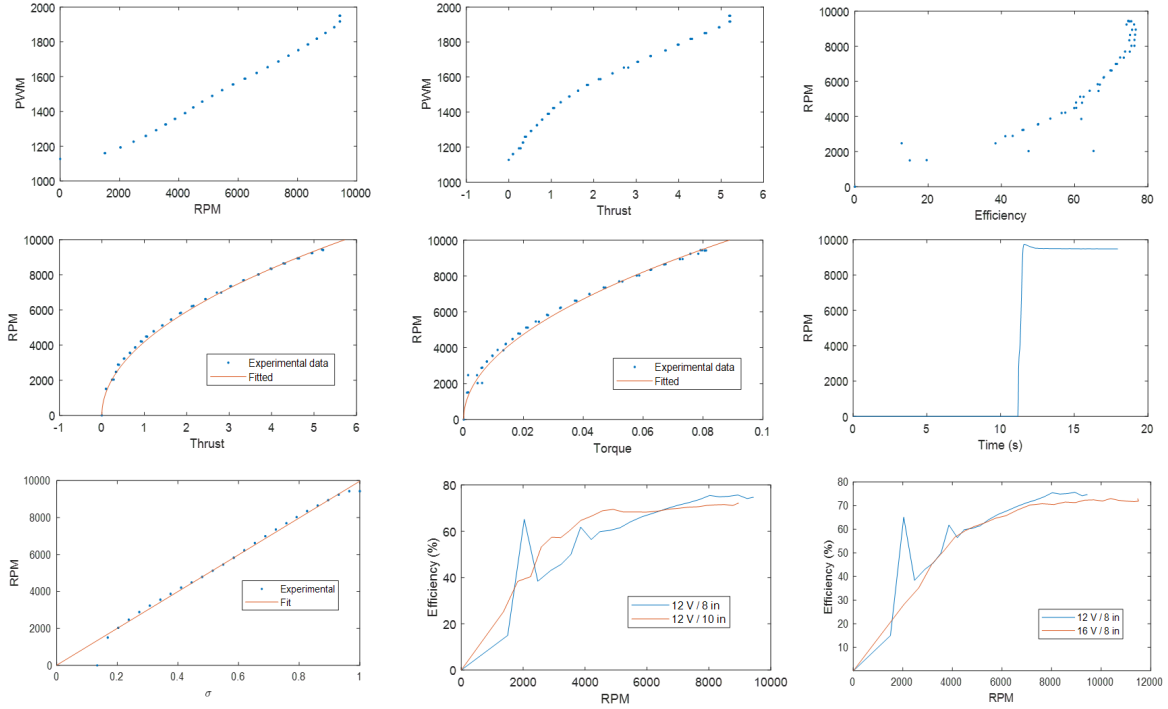


Figure 27: Dynamometer experimental results. Propulsion system parameters were obtained through a least squares curve fit.

existence of a dead zone for low  $\sigma$  and saturation for high  $\sigma$ . This wasn't problematic since quadcopters do not usually operate in those zones while flying.

Finally, the propeller experienced some transient behavior until it reached the steady state  $\omega_{ss}$  given by Eq. (38). This was modeled as a low pass filter with time constant  $T_m$ :

$$\omega = \frac{1}{T_m s + 1} \omega_{ss}. \quad (39)$$

The time constant  $T_m$  was obtained by analyzing the step response of the system (see Fig. 27). Note that  $T_m$  is the time that the system in Eq. 39 needs to reach 63.2% of the final step value.

The following plots have been included in this section:

- RPM versus PWM, Thrust versus PWM, Efficiency versus RPM, Thrust versus RPM, Torque versus RPM, Step Response,  $\sigma$  versus RPM for 3S batteries and 8 inch propellers.
- RPM versus Efficiency compares different combinations of batteries and propeller size. The efficiency peak that appears at 2000 RPM for the 12 V / 8 inch curve is because the motor's mechanical power output is very low at

low RPM. Then, for a range of RPM around 2000, it increases much faster than the electrical power provided to the motor, generating the peak.

From these plots, it was determined that a larger propeller (10 inches) was better for efficiency because bigger propellers have a larger surface in contact with the air. In general, larger propellers paired with lower KV motors are more efficient than shorter propellers matched with higher KV motors. The testing quadcopter had a constraint on propeller size due to the propeller guards. Thus, the 8 inch propeller was chosen.

Regarding battery voltage, it is desirable that, should a designer choose a higher battery voltage, a smaller propeller size should be used. The loss of efficiency at high RPM with the 16 V battery may have been due to the increased energy losses.

In summary, the pairing of a 12 V battery, motor, and 8-in propeller was adequate for the quadcopter as it provided a reasonable efficiency (around 70%) for the expected typical flight condition.

The mass and inertia were computed using two methods, namely a lumped mass model, and by measuring the physical properties using a scale and

a bifilar pendulum.

The total mass of the quadcopter as determined by each method was the following:

$$m_{\text{lumped model}} = 0.997 \text{ kg}, \quad m_{\text{scale}} = 1.062 \text{ kg}$$

The inertia tensor (in  $kg \cdot m^2$ ) computed with the lumped mass model was as follows

$$J = \begin{bmatrix} 0.0109 & -4.3412 \cdot 10^{-6} & 3.6716 \cdot 10^{-5} \\ -4.3412 \cdot 10^{-6} & 0.0109 & -2.2186 \cdot 10^{-5} \\ 3.6716 \cdot 10^{-5} & -2.2186 \cdot 10^{-5} & 0.0200 \end{bmatrix}.$$

The products of inertia were assumed to be zero due to the symmetry in the mass configuration of the quadcopter. The moments of inertia were computed using the bifilar pendulum method. If the pendulum period is  $T_{\text{pend}}$ , then the moment of inertia will be given by

$$J = \frac{mgd^2}{16\pi^2 L} T_{\text{pend}}^2. \quad (40)$$

To determine the pendulum period, two methods were used (see Fig. 28):

1. Inspection of the Time versus Orientation plot.
2. Computation of the periodogram of the Time versus Orientation plot and identification of the pendulum period from the peak.

Both methods yielded very similar results, so, in the end, 1) was arbitrarily chosen. The resulting moments of inertia (in  $kg \cdot m^2$ ) were:

$$J_{xx} = 0.0107, \quad J_{yy} = 0.0111, \quad J_{zz} = 0.0229.$$

Note how similar the results were between the lumped mass model and the bifilar pendulum experiments. The differences among them were attributed to erroneous and noisy measurements of distance, weight, and pendulum period.

## B. Vertical Position & Velocity Estimator

### B.1. Discrete Gauss-Markov Prediction Model

$$\begin{bmatrix} z_{k+1} \\ \dot{z}_{k+1} \\ \ddot{z}_{\text{bias},k+1} \end{bmatrix} = \begin{bmatrix} 1 & T_s & 0 \\ 0 & 1 & -T_s \\ 0 & 0 & 1 \end{bmatrix} \begin{bmatrix} z_k \\ \dot{z}_k \\ \ddot{z}_{\text{bias},k} \end{bmatrix} + \begin{bmatrix} \frac{T_s^2}{2m} \\ \frac{T_s}{m} \\ 0 \end{bmatrix} (-\ddot{z}_k - g) + \begin{bmatrix} \frac{T_s^2}{2m} \\ \frac{T_s}{m} \\ 0 \end{bmatrix} w_{\ddot{z}_k}, \quad (41)$$

where  $\ddot{z}_{\text{bias},k}$  is the estimated accelerometer bias in the  $z$ -axis at step  $k$  and  $w_{\ddot{z}_k}$  represents the process noise that acts upon the acceleration  $\ddot{z}$  at step  $k$ .

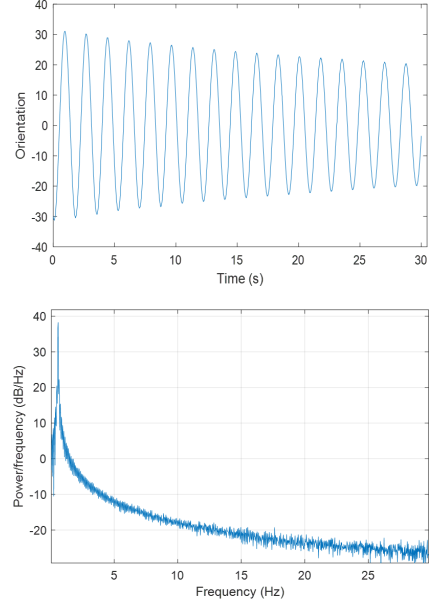


Figure 28: Results of the bifilar pendulum experiment for the characterization of  $J_{zz}$ . The top plot is the orientation of the drone against time, the bottom plot is the periodogram of the time series given by the top plot.

### B.2. Discrete Gauss-Markov Measurement Model

$$\begin{bmatrix} z_{\text{baro},k} \\ z_{\text{rf},k} \\ z_{\text{MOCAP},k} \end{bmatrix} = \begin{bmatrix} -1 & 0 & 0 \\ -1 & 0 & 0 \\ -1 & 0 & 0 \end{bmatrix} \begin{bmatrix} z_k \\ \dot{z}_k \\ \ddot{z}_{\text{bias},k} \end{bmatrix} + \begin{bmatrix} b_{\text{baro}} \\ b_{\text{rf}} \\ 0 \end{bmatrix} + \begin{bmatrix} n_{\text{baro}} \\ n_{\text{rf}} \\ n_{z,\text{MOCAP}} \end{bmatrix} \quad (42)$$

where  $z_{\text{baro},k}$ ,  $z_{\text{rf},k}$ , and  $z_{\text{MOCAP},k}$  are, respectively, the barometer, range finder, and MOCAP altitude measurements at step  $k$ ,  $b_{\text{baro}}$  and  $b_{\text{rf}}$  are, respectively, the barometer and range finder biases, and  $n_{\text{baro}}$ ,  $n_{\text{rf}}$ , and  $n_{z,\text{MOCAP}}$  represent, respectively, the barometer, range finder, and MOCAP sensor noise that acts upon the altitude measurements.

### B.3. Covariance Matrices

The process covariance matrix  $W$  was given by

$$W = \text{diag}([0, \quad 0.1428, \quad 0.1]).$$

The sensor noise covariance matrix  $V$  was given by

$$V = \text{diag}([1.00 \cdot 10^6, \quad 1.20 \cdot 10^{-6}, \quad 10^{-4}]).$$

## C. Horizontal Position & Velocity Estimator

### C.1. Discrete Gauss-Markov Prediction Model

$$\begin{bmatrix} x_{k+1} \\ y_{k+1} \\ \dot{x}_{k+1} \\ \dot{y}_{k+1} \\ \ddot{x}_{\text{bias},k+1} \\ \ddot{y}_{\text{bias},k+1} \end{bmatrix} = \begin{bmatrix} 1 & 0 & T_s & 0 & 0 & 0 \\ 0 & 1 & 0 & T_s & 0 & 0 \\ 0 & 0 & 1 & 0 & -T_s & 0 \\ 0 & 0 & 0 & 1 & 0 & -T_s \\ 0 & 0 & 0 & 0 & 1 & 0 \\ 0 & 0 & 0 & 0 & 0 & 1 \end{bmatrix} \begin{bmatrix} x_k \\ y_k \\ \dot{x}_k \\ \dot{y}_k \\ \ddot{x}_{\text{bias},k} \\ \ddot{y}_{\text{bias},k} \end{bmatrix} + \begin{bmatrix} \frac{T_s^2}{2m} & 0 \\ 0 & \frac{T_s^2}{2m} \\ \frac{T_s}{m} & 0 \\ 0 & \frac{T_s}{m} \\ 0 & 0 \\ 0 & 0 \end{bmatrix} \begin{bmatrix} \ddot{x}_k \\ \ddot{y}_k \end{bmatrix} + \begin{bmatrix} \frac{T_s^2}{2m} & 0 \\ 0 & \frac{T_s^2}{2m} \\ \frac{T_s}{m} & 0 \\ 0 & \frac{T_s}{m} \\ 0 & 0 \\ 0 & 0 \end{bmatrix} \begin{bmatrix} w_{\ddot{x}_k} \\ w_{\ddot{y}_k} \end{bmatrix}, \quad (43)$$

where  $\ddot{x}_{\text{bias},k}$  and  $\ddot{y}_{\text{bias},k}$  are the estimated accelerometer biases at step  $k$  in the  $x$ -axis and  $y$ -axis respectively, and  $w_{\ddot{x}_k}$  and  $w_{\ddot{y}_k}$  represent the process noise at step  $k$  that acts upon the accelerations  $\ddot{x}$  and  $\ddot{y}$  respectively.

### C.2. Discrete Gauss-Markov Measurement Model

$$\begin{bmatrix} x_{\text{MOCAP},k} \\ y_{\text{MOCAP},k} \end{bmatrix} = \begin{bmatrix} 1 & 0 & 0 & 0 & 0 & 0 \\ 0 & 1 & 0 & 0 & 0 & 0 \end{bmatrix} \begin{bmatrix} x_k \\ y_k \\ \dot{x}_k \\ \dot{y}_k \\ \ddot{x}_{\text{bias},k} \\ \ddot{y}_{\text{bias},k} \end{bmatrix} + \begin{bmatrix} n_{x,\text{MOCAP}} \\ n_{y,\text{MOCAP}} \end{bmatrix} \quad (44)$$

where  $x_{\text{MOCAP},k}$  and  $y_{\text{MOCAP},k}$  are, respectively, the MOCAP  $x$ -axis and  $y$ -axis position measurements at step  $k$ , and  $n_{x,\text{MOCAP}}$  and  $n_{y,\text{MOCAP}}$  represent the MOCAP sensor noise that acts upon the  $x$ -axis and  $y$ -axis position measurements respectively.

### C.3. Covariance Matrices

The process covariance matrix  $W$  was given by

$$W = \text{diag}([0, 0, 0.2749, 0.0328, 0.1, 0.1]).$$

The sensor noise covariance matrix  $V$  was given by

$$V = \text{diag}([10^{-4}, 10^{-4}]).$$

## D. Yaw & Yaw Rate Estimator

### D.1. Discrete Gauss-Markov Prediction Model

$$\begin{bmatrix} \psi_{k+1} \\ \omega_{z,k+1}^b \\ \omega_{z,\text{bias},k+1}^b \end{bmatrix} = \begin{bmatrix} 1 & T_s & -T_s \\ 0 & 1 & 0 \\ 0 & 0 & 1 \end{bmatrix} \begin{bmatrix} \psi_k \\ \omega_{z,k}^b \\ \omega_{z,\text{bias},k}^b \end{bmatrix}, \quad (45)$$

where  $\omega_{z,\text{bias},k}^b$  is the rate gyro bias around the  $z$ -axis at step  $k$ .

### D.2. Discrete Gauss-Markov Measurement Model

$$\begin{bmatrix} \psi_{\text{MOCAP},k} \\ \omega_{z,\text{gyro},k}^b \end{bmatrix} = \begin{bmatrix} 1 & 0 & 0 \\ 0 & 1 & 0 \end{bmatrix} \begin{bmatrix} \psi_k \\ \omega_{z,k}^b \\ \omega_{z,\text{bias},k}^b \end{bmatrix} + \begin{bmatrix} n_{\psi,\text{MOCAP}} \\ n_{\text{gyro}} \end{bmatrix}, \quad (46)$$

where  $\psi_{\text{MOCAP},k}$ , and  $\omega_{z,\text{gyro},k}^b$  are, respectively, the MOCAP yaw and the rate gyro yaw rate measurements at step  $k$ , and  $n_{\psi,\text{MOCAP}}$ , and  $n_{\text{gyro}}$  represent, respectively, the MOCAP and rate gyro sensor noise that acts upon the yaw and yaw rate measurements.

### D.3. Covariance Matrices

The process covariance matrix  $W$  was given by

$$W = \text{diag}([0, 0, 0.1]).$$

The sensor noise covariance matrix  $V$  was given by

$$V = \text{diag}([10^{-4}, -0.7822]).$$

## E. Sensor Calibration Results

Covariances used in-flight for motion capture measurements were set to higher than measured values to assure the Kalman Filter correction step would not operate on near-singular matrices. The motion capture biases were assumed to be zero because the camera system was calibrated before use. Accelerometer and gyro biases and slopes were originally determined from linear least squares fits on rate table experimental data as shown in Table 10. In practice, the biases were estimated on-the-fly with Kalman Filters.

## References

- Abdolkhosseini, M., Zhang, Y.M., Rabbath, C.A., 2013. An efficient model predictive control scheme for an unmanned quadrotor helicopter. *Journal of Intelligent & Robotic Systems* 70, 27–38.
- Al Younes, Y., Drak, A., Noura, H., Rabhi, A., El Hajjaji, A., 2016. Robust model-free control applied to a quadrotor uav. *Journal of Intelligent & Robotic Systems* 84, 37–52.
- Alexis, K., Nikolakopoulos, G., Tzes, A., 2010. Constrained optimal attitude control of a quadrotor helicopter subject to wind-gusts: Experimental studies, in: *Proceedings of the 2010 American Control Conference*, pp. 4451–4455.
- Åström, K.J., Häggglund, T., 1995. *PID controllers: theory, design, and tuning*. volume 2. Instrument society of America Research Triangle Park, NC.
- Bangura, M., Mahony, R., 2014. Real-time model predictive control for quadrotors. *IFAC Proceedings Volumes* 47, 11773 – 11780. 19th IFAC World Congress.

Table 10: Sensor Calibration Results

Sensor	Covariance Measured	Covariance Used	Bias	Slope
Accelerometer $\ddot{x}^b$	0.2749 m <sup>2</sup>	Same	7 MPU Counts	417.30 (m/s <sup>2</sup> )/MPU Count
Accelerometer $\ddot{y}^b$	0.0328 m <sup>2</sup>	Same	73 MPU Counts	417.83 (m/s <sup>2</sup> )/MPU Count
Accelerometer $\ddot{z}^b$	0.1428 m <sup>2</sup>	Same	-36 MPU Counts	419.84 (m/s <sup>2</sup> )/MPU Count
Rate Gyro $\omega_x^b$	0.8747 (deg/s) <sup>2</sup>	Not Used	-1 MPU Count	16.325 (deg/s)/MPU Count
Rate Gyro $\omega_y^b$	0.7486 (deg/s) <sup>2</sup>	Not Used	0 MPU Counts	16.394 (deg/s)/MPU Count
Rate Gyro $\omega_z^b$	0.7822 (deg/s) <sup>2</sup>	Same	-11 MPU Counts	16.378 (deg/s)/MPU Count
Barometer $z$	0.0552 m <sup>2</sup>	10 <sup>6</sup> m <sup>2</sup>	Avg. of 50 samples	N/A
Range Finder $z^b$	1.20 · 10 <sup>-6</sup> m <sup>2</sup>	Same	Avg. of 10 samples	N/A
Motion Capture $x^i$	2.25 · 10 <sup>-10</sup> m <sup>2</sup>	10 <sup>-4</sup> m <sup>2</sup>	0	N/A
Motion Capture $y^i$	2.89 · 10 <sup>-10</sup> m <sup>2</sup>	10 <sup>-4</sup> m <sup>2</sup>	0	N/A
Motion Capture $z^i$	7.84 · 10 <sup>-10</sup> m <sup>2</sup>	10 <sup>-4</sup> m <sup>2</sup>	0	N/A
Motion Capture $\psi$	Not measured	10 <sup>-4</sup> m <sup>2</sup>	0	N/A

- Bekcheva, M., Join, C., Mounier, H., 2018. Cascaded model-free control for trajectory tracking of quadrotors, in: 2018 international conference on unmanned aircraft systems (ICUAS), IEEE. pp. 1359–1368.
- Bolandi, H., Rezaei, M., Mohsenipour, R., Nemati, H., Smailzadeh, S.M., 2013. Attitude control of a quadrotor with optimized pid controller. *Intelligent Control and Automation* 4, 335.
- Bouabdallah, S., Siegwart, R., 2007. Full control of a quadrotor, in: 2007 IEEE/RSJ International Conference on Intelligent Robots and Systems, pp. 153–158.
- Cairano, S.D., Bemporad, A., 2009. Model predictive controller matching: Can mpc enjoy small signal properties of my favorite linear controller? 2009 European Control Conference (ECC) , 2217–2222.
- Danielson, C., Borrelli, F., 2015. Symmetric linear model predictive control. *IEEE Transactions on Automatic Control* 60, 1244–1259.
- Dong, W., Gu, G.Y., Zhu, X., Ding, H., 2013. Modeling and control of a quadrotor uav with aerodynamic concepts, in: Proceedings of World Academy of Science, Engineering and Technology, World Academy of Science, Engineering and Technology (WASET). p. 437.
- Heng, X., Cabecinhas, D., Cunha, R., Silvestre, C., Qingsong, X., 2015. A trajectory tracking lqr controller for a quadrotor: Design and experimental evaluation, in: TENCON 2015-2015 IEEE Region 10 Conference, IEEE. pp. 1–7.
- Hoffmann, G., Huang, H., Waslander, S., Tomlin, C., 2007. Quadrotor helicopter flight dynamics and control: Theory and experiment. *AIAA Guidance, Navigation and Control Conference and Exhibit* .
- Huang, H., Hoffmann, G.M., Waslander, S.L., Tomlin, C.J., 2009. Aerodynamics and control of autonomous quadrotor helicopters in aggressive maneuvering, in: 2009 IEEE international conference on robotics and automation, IEEE. pp. 3277–3282.
- Kamel, M., Stastny, T., Alexis, K., Siegwart, R., 2017. Model predictive control for trajectory tracking of unmanned aerial vehicles using robot operating system, in: Koubaa, A. (Ed.), *Robot Operating System (ROS): The Complete Reference (Volume 2)*. Springer International Publishing, Cham, pp. 3–39.
- Kwakernaak, H., Sivan, R., 1972. *Linear optimal control systems*. volume 1. Wiley-interscience New York.
- Liao-McPherson, D., Nicotra, M.M., Kolmanovsky, I., 2020. Time-distributed optimization for real-time model predictive control: Stability, robustness, and constraint satisfaction. *Automatica* 117, 108973.
- Liu, C., Lu, H., Chen, W.H., 2015. An explicit mpc for quadrotor trajectory tracking, in: 2015 34th Chinese Control Conference (CCC), IEEE. pp. 4055–4060.
- Mayne, D.Q., Rawlings, J.B., Rao, C.V., Sokaert, P.O., 2000. Constrained model predictive control: Stability and optimality. *Automatica* 36, 789 – 814.
- Paredes, J.A., Saito, C., Abarca, M., Cuellar, F., 2017. Study of effects of high-altitude environments on multi-copter and fixed-wing uavs’ energy consumption and flight time, in: 2017 13th IEEE Conference on Automation Science and Engineering (CASE), pp. 1645–1650.
- Powers, C., Mellinger, D., Kumar, V., 2015. Quadrotor kinematics and dynamics, in: Valavanis, K.P., Vachtsevanos, G.J. (Eds.), *Handbook of Unmanned Aerial Vehicles*. Springer Netherlands, Dordrecht, pp. 307–328.
- Quan, Q., 2017. *Introduction to multicopter design and control*. Springer.
- Reyes-Valeria, E., Enriquez-Caldera, R., Camacho-Lara, S., Guichard, J., 2013. Lqr control for a quadrotor using unit quaternions: Modeling and simulation, in: CONIELECOMP 2013, 23rd International Conference on Electronics, Communications and Computing, pp. 172–178.
- Romano, M., Kuevor, P., Lukacs, D., Marshall, O., Stevens, M., Rastgoftar, H., Cutler, J., Atkins, E., 2019. Experimental evaluation of continuum deformation with a five quadrotor team, in: 2019 American Control Conference (ACC), pp. 2023–2029.
- Sontag, E.D., 1990. *Optimal Control*. Springer US, New York, NY. pp. 273–318.
- Waslander, S., Wang, C., 2009. Wind disturbance estimation and rejection for quadrotor position control, in: *AIAA Infotech@Aerospace Conference*.
- Yun Li, Kiam Heong Ang, Chong, G.C.Y., 2006. Pid control system analysis and design. *IEEE Control Systems Magazine* 26, 32–41.



**Juan Paredes** received the B.Sc. degree in mechatronics engineering from the Pontifical Catholic University of Peru and a M.Sc. degree in aerospace engineering from the University of Michigan in Ann Arbor, MI. He

is currently a PhD candidate in the Aerospace Engineering Department at the University of Michigan. His interests are in autonomous flight control and control of combustion.



**Prashin Sharma** is currently pursuing his PhD in Robotics from University of Michigan, Ann Arbor. His research is focused on prognostics informed decision making for safe autonomous drone flights. He has a combined work experience of six years in industries spanning from flat panel OLED displays

to security. He holds a BE in Mechanical Engineering from Mumbai University and MS in Mechanical Engineering from Carnegie Mellon University.



**Brian Ha** is a professional aerospace engineer. His work experience includes satellite flight operations with Google Inc. and launch vehicle design with Northrop Grumman. He received his B.S. in Aerospace Engineering from San José State University in 2015 and

his M.S.E. in Aerospace Engineering from the University of Michigan in 2019. He specializes in the practical implementation of state estimation, constrained feedback control, and real-time optimization on embedded systems.



**Manuel Lanchares** is a PhD student in Aerospace Engineering at the Georgia Institute of Technology, where his research is focused on stochastic nonlinear control. His work experience includes computation of aircraft performance specifications and

implementation of nonlinear methods for orbital covariance propagation. He received the BS in Aerospace Engineering from the Technical University of Madrid in 2016, the MS in Mathematical Engineering from Complutense University of Madrid in 2017, and the MSE in Aerospace Engineering from the University of Michigan in 2019.



**Ella Atkins** is a Professor of Aerospace Engineering at the University of Michigan, where she directs the Autonomous Aerospace Systems Lab. Dr. Atkins holds B.S. and M.S. degrees in Aeronautics and Astronautics from MIT and M.S. and

Ph.D. degrees in Computer Science and Engineering from the University of Michigan. She is Editor-in-Chief of the AIAA Journal of Aerospace Information Systems (JAIS) and has served on the National Academy's Aeronautics and Space Engineering Board, the Institute for Defense Analysis Defense Science Studies Group, and in multiple AIAA technical committees. She pursues research in Aerospace system autonomy and safety and is currently engaged as a Technical Fellow at Collins Aerospace.



**Peter Gaskell** is a Lecturer and Adjunct Researcher at the University of Michigan Robotics Institute, where he develops robotics platforms for both education and research. He researches efficient algorithms for

localization and navigation of autonomous systems. Dr. Gaskell holds a B.S. degree in Physics from the University of Oregon, and M.Eng. and Ph.D. degrees in Electrical Engineering from McGill University.



**Ilya Kolmanovsky** is a professor in the department of aerospace engineering at the University of Michigan, with research interests in control theory for systems with state and control constraints, and in control

applications to aerospace and automotive systems. He received his Ph.D. degree from the University of Michigan in 1995. He is a Fellow of IEEE and is named as an inventor on over 100 United States patents.